SMAP retrieval assimilation improves soil moisture estimation across irrigated areas in South Asia

Jawairia A. Ahmad[1], Barton A. Forman[1], and Sujay V. Kumar[2]

[1]Department of Civil and Environmental Engineering, University of Maryland, College Park, MD 20742, USA
[2]Hydrological Sciences Laboratory, NASA Goddard Space Flight Center, Greenbelt, MD 20771, USA

Correspondence: Jawairia A. Ahmad (jahmad@umd.edu)

Abstract. A soil moisture retrieval assimilation framework is implemented across South Asia in an attempt to improve regional soil moisture estimation as well as to provide a consistent regional soil moisture dataset. This study aims to improve the spatiotemporal variability of soil moisture estimates by assimilating Soil Moisture Active Passive (SMAP) near surface soil moisture retrievals into a land surface model. The Noah-MP (v4.0.1) land surface model is run within the NASA Land Information System software framework to model regional land surface processes. NASA Modern-Era Retrospective Analysis for
5 Research and Applications (MERRA2) and GPM Integrated Multi-satellitE Retrievals (IMERG) provide the meteorological boundary conditions to the land surface model. Assimilation is carried out using both cumulative distribution function (CDF) corrected (DA-CDF) and uncorrected SMAP retrievals (DA-NoCDF). CDF-matching is implemented to map the statistical moments of the SMAP soil moisture retrievals to the land surface model climatology. Comparison of assimilated and model-only soil moisture estimates with publicly available in-situ measurements highlight the relative improvement in soil moisture
10 estimates by assimilating SMAP retrievals. Across the Tibetan Plateau, DA-NoCDF reduced the mean bias and RMSE by 8.4% and 9.4% even though assimilation only occurred during less than 10% of the study period due to frozen soil conditions. The best goodness-of-fit statistics were achieved for the IMERG DA-NoCDF soil moisture experiment. SMAP retrieval assimilation corrected biases associated with unmodeled hydrologic phenomenon (e.g., anthropogenic influences due to irrigation). The highest influence of assimilation was observed across croplands. Improvements in soil moisture translated into improved
15 spatiotemporal patterns of modeled evapotranspiration, yet limited influence of assimilation was observed on states included within the carbon cycle such as gross primary production. Improvement in fine-scale modeled estimates by assimilating coarse-scale retrievals highlights the potential of this approach for soil moisture estimation over data scarce regions.

1 Introduction

20 Soil moisture (SM) is an important variable in geophysical science. In land surface models, soil moisture primarily influences the energy cycle by controlling latent heat flux and soil temperature (Al-Kayssi et al., 1990), and the water cycle via evapotranspiration, soil infiltration capacity, and runoff (Penna et al., 2011). Accurate soil moisture estimation is also a requirement for analyzing the effects of climate change as soil moisture variability influences terrestrial carbon uptake (Green et al., 2019). In the context of agriculture, soil moisture provides a quantitative basis for the development of sociopolitical policies aimed

25 at regulating and monitoring crop cultivation, crop selection, water resources distribution, and irrigation processes (Schneider, 1989; Shani et al., 2004; Jalilvand et al., 2019). Soil moisture-based frameworks have been extensively used for irrigation scheduling and monitoring, particularly in terms of tracking plant growth (Dukes and Scholberg, 2005; Soulis et al., 2015). The three main sources of surface soil moisture are precipitation (Morin and Benyamini, 1977; Douville et al., 2001; Wei and Dirmeyer, 2012), runoff (Daly and Porporato, 2005), and surface irrigation via groundwater pumping. The feedback loop
30 between soil moisture and each of these sources varies in space and time according to the geographic and topological features of the locale (Wei and Dirmeyer, 2012).

Various techniques have been used in soil moisture estimation such as in situ station networks, physical modeling, and remote sensing (Seneviratne et al., 2010; Hauser et al., 2017; Reichle et al., 2021). While the in situ station data is considered most representative of the true ground conditions, it is generally limited by spatiotemporal data sparsity issues. In contrast,
35 physical modeling can be leveraged to provide estimates at fine spatiotemporal resolutions. However, contemporary modeling techniques lack comprehensive representation of the complex relationships between all geophysical variables. Remote sensing has also been widely utilized in soil moisture estimation to translate optical (Piles et al., 2011), thermal infrared (Zhang et al., 2014), and microwave radiation (Entekhabi et al., 2010; Panciera et al., 2013) data into soil moisture retrievals.

While providing useful information, remote sensing-based soil moisture retrievals are limited by the accuracy of the retrieval
40 algorithm, swath width, field-of-view, and the orbital specifications of the observing instrument (aboard the satellite). One effective method for overcoming the limitations posed by physical modeling and remote sensing sensors is data assimilation. Data assimilation (DA) is a technique used to merge modeled estimates with observations while taking into consideration their respective errors and uncertainties (Kalman, 1960; McLaughlin, 2002). The posterior estimate obtained through DA combines the strengths of both models and observations to yield a dataset that is improved relative to the standalone products (Zhang and
45 Moore, 2015). Several studies have attempted to improve water budget estimation by assimilating soil moisture observations into land surface model (LSM) estimates. Huang et al. (2008) assimilated in situ surface soil moisture measurements and low-frequency PMW remote sensing data into the Simple Biosphere Model (SiB2) and produced improvements in surface soil moisture estimates. Lievens et al. (2015) modeled the hydrologic cycle over the Murray Darling Basin in Australia and explored the results of assimilating Soil Moisture and Ocean Salinity (SMOS) soil moisture retrievals into the Variable Infiltration
50 Capacity (VIC) model. They concluded that improvements in the wetness conditions due to soil moisture retrieval assimilation translated into improved predictions of associated water fluxes. Comparison of modeled soil moisture estimates with soil moisture retrievals revealed an inherent bias in the statistical moments of the studied retrievals (Reichle et al., 2004). A bias correction technique based on CDF-matching suggested by Reichle and Koster (2004) demonstrated better conformity in the statistical moments between the LSM soil moisture estimates and the satellite-based soil moisture retrievals. However,
55 Kumar et al. (2015) showed that retrieval distribution mapping via CDF-matching could result in the removal of information pertaining to the irrigation signal. Nearing et al. (2018) also attributed loss of signal information to CDF-matching during data assimilation.

According to the current climate change forecasts, severe water stress is predicted in various parts of South Asia (Sivakumar and Stefanski, 2010). Total groundwater storage in northwestern India has undergone a decline, which is likely linked

60   to irrigation-induced groundwater pumping (Rodell et al., 2009; Asoka et al., 2017). Global land surface models (LSM), in general, do not include groundwater pumping modules. An inverse technique of estimating the amount of groundwater pumped could potentially be developed if accurate soil moisture estimates are available (apart from the other water budget contributing variables). Soil moisture records may be able to provide the much needed information about the extent and amount of groundwater pumping across the whole of South Asia. Accurate soil moisture estimation across South Asia is, therefore, an important

65   need.

     In situ soil moisture measurements across South Asia are scarce (apart from having limited accessibility). To fill this knowledge gap and to evaluate the utility of leveraging data assimilation as a feasible option in this region, we demonstrate the utilization of Soil Moisture Active Passive (SMAP; Entekhabi et al. (2010)) retrieval assimilation to improve soil moisture estimation across South Asia. Section 2 describes the prominent features of the study domain; Sect. 3 provides details re-

70   garding the various datasets and the data assimilation framework utilized; Sect. 4 highlights the important results of the DA experiments; and Sect. 5 summarizes the main conclusions of this study.

2   Study domain

The study domain discussed in this paper encompasses the mountainous region in South Asia and the adjoining areas, Fig. 1. The HinduKush-Himalayan mountain range and the Tibetan Plateau, represented by grid cells with elevation > 2000 m in Fig.

75   1(a) constitute high mountain Asia. Ten major rivers (Indus, Ganges, Brahmaputra, Irrawaddy, Salween, Mekong, Yangtze, Yellow, Tarim, Amu, and Syr) originate in this region and flow towards the low elevation areas where they serve as sources of freshwater for the residing populace. Agriculture-based irrigation is a primary consumer of the freshwater transported downstream by the rivers (Wester et al., 2018).

     Figure 1(c) and Table A1 present the soil texture conditions within the domain. The NCEP/STATSGO+FAO (Natural Re-

80   sources Conservation Service) soil texture classification is used to categorize the grid cells into 16 individual classes (Note: soil classes that did not have any grid cell types in the study domain are excluded from the figure legend). The predominant soil texture type found within the domain is loam followed by clay loam. Landcover categorization (see Fig. 1(d) and Table A1 columns 4 to 6) is based on the NCEP/MODIS-based International Geosphere–Biosphere Programme (IGBP) (Friedl et al., 2002) classification (Note: similar classes are lumped together, for example different forest types are grouped into a singular

85   forest class). The predominant landcover types present within the study domain are barren, croplands, and shrublands.

     The Food and Agriculture Organization (FAO) of the United Nations provides a global map of fraction areas that are equipped for irrigation as part of the Global Map of Irrigation Areas (GMIA) product, which is provided at a 5-arc minute (0.0833°) resolution (Siebert et al., 2005). The GMIA product was used in this study to represent the total irrigation-equipped area within each grid cell, see Fig. 7(c). The grid cells with high irrigation percentages correspond well (spatially) with grid

90   cells belonging to the landcover type croplands in Fig. 1(d).
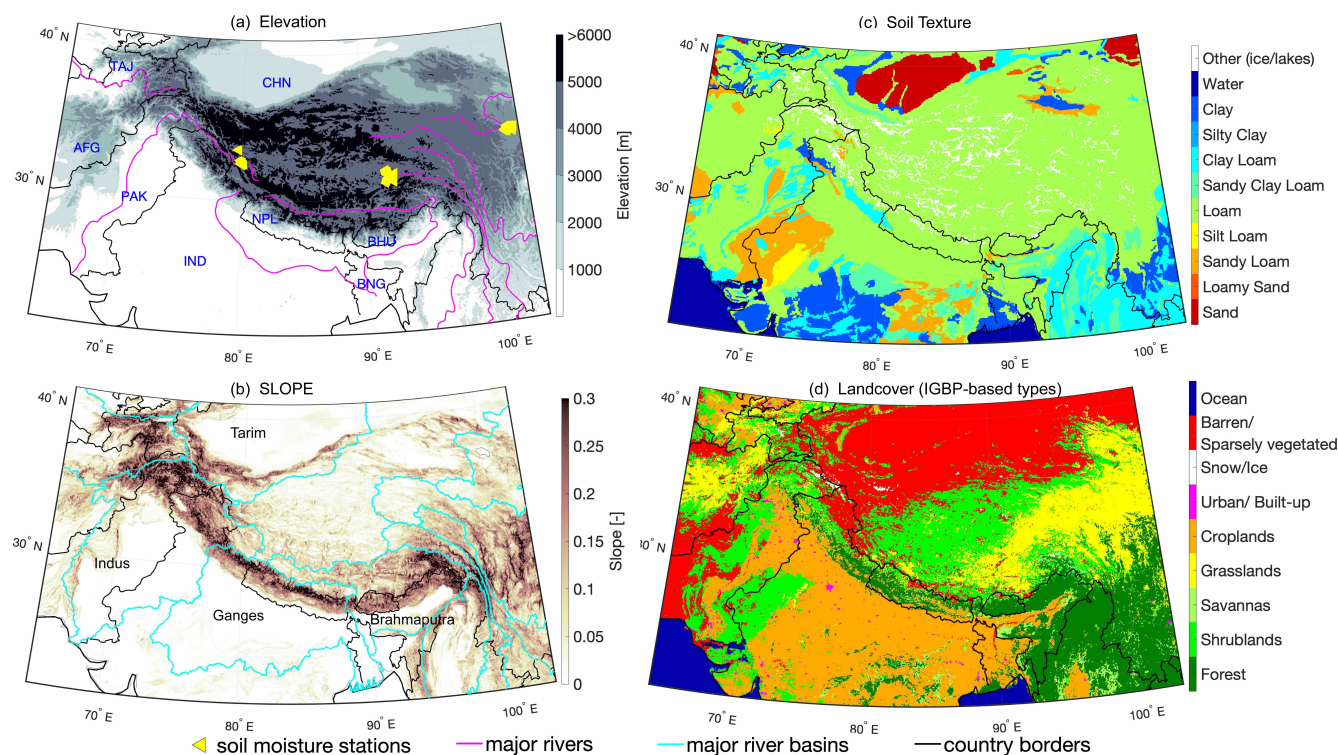
Figure 1. The study domain encompasses the mountainous region in South Asia and the adjoining areas. High elevation and high slope (>0.2) areas demarcate the HinduKush-Himalayan mountain ranges, whereas the high elevation and mild slope (<0.1) grid cells demarcate the Tibetan Plateau (subplots (a) and (b)). The yellow markers in subplot (a) locate the stations within the Tibetan Plateau used to evaluate the soil moisture estimates (Sect. 4.1). The domain soil texture was categorized into 11 soil types (subplot c) according to the NCEP/STATSGO+FAO classification. The domain landcover comprised 10 main types based on the MODIS-derived IGBP classification (subplot d). AFG= Afghanistan, BNG= Bangladesh, BHU= Bhutan, CHN= China, IND= India, NPL= Nepal, PAK= Pakistan, and TAJ= Tajikistan.

3 Methodology and datasets

This section describes the methodology developed to implement the assimilation of SMAP soil moisture retrievals into the land surface model as well as the various datasets utilized in the analysis results detailed in Sect. 4.

3.1 NASA Land Information System

95   The NASA Land Information System (LIS) is a software framework which facilitates high performance computing for land surface modeling and data assimilation purposes (Kumar et al., 2006; Peters-Lidard et al., 2007). The NASA LIS framework was used to run the Noah-MP land surface model (LSM) and to assimilate SMAP soil moisture retrievals (Fig. 2).

Table 1. Selection of model components in Noah-MP version 4.0.1 as implemented within LIS (Sect. 3.1.1).

Model Components	Selected Inputs or Parameterizations
Elevation, slope, and aspect	SRTM30-v2.0 (Farr et al., 2007)
Landcover	MODIS (IGBP-NCEP) (Friedl et al., 2002)
Maximum albedo	National Centers for Environmental Prediction (Robinson and Kukla, 1985)
Greenness	National Centers for Environmental Prediction (Gutman and Ignatov, 1998)
Vegetation	Dynamic vegetation option
Canopy stomatal resistance	Ball-Berry method (Ball et al., 1987)
Runoff and groundwater	Simple groundwater model, SIMGM (Niu et al., 2007)
Supercooled liquid water and frozen soil permeability	NY06 (Niu and Yang, 2006)
Surface-layer drag coefficient	General Monin-Obukhov similarity theory (Brutsaert, 2013)
Snow surface albedo	Biosphere-Atmosphere Transfer Scheme (Yang and Dickinson, 1996)
Partitioning of rain and snowfall	Jordan91 (Jordan, 1991)
Snow and soil temperature	Semi-implicit option
Lower boundary of soil temperature	Noah native option
Meteorological boundary conditions	MERRA-2 (Gelaro et al., 2017), IMERG (Huffman et al., 2015)

3.1.1 Noah-MP land surface model

The Noah-MP (version 4.0.1) LSM (Ek et al., 2003; Niu et al., 2011; Yang et al., 2011) was run within LIS to simulate the
100 relevant land surface processes across the study domain. Noah-MP was run on an equidistant cylindrical grid with a spatial
resolution of 0.05° x 0.05° at a 15 minute timestep. Table 1 outlines the Noah-MP physics in this study.

Noah-MP was selected for this study due to the multilayer representation of soil, explicit modeling of frozen soil permeability
(Niu and Yang, 2006), and representation of snowpack and soil interface processes. Noah-MP (version 4.0.1) includes coupled
energy, water, and carbon cycle simulation routines. The soil profile is divided into four layers with thicknesses of 5, 35, 60,
105 and 100 cm, respectively. A three-layer (maximum) snow structure is implemented above the surface soil layer to capture
snowpack dynamics and the snowpack-soil interface fluxes for areas that experience snowfall (Niu et al., 2011). Noah-MP
was (separately) forced with meteorological fields from Modern-Era Retrospective analysis for Research and Applications
(MERRA2, Gelaro et al. (2017)) and Integrated Multi-satellite Retrievals for Global Precipitation Measurement (IMERG,
Huffman et al. (2015)). The IMERG Final run was used. External irrigation and groundwater pumping were not explicitly
110 modeled. Thus, there was an information gap regarding these two water sources in the modeled water cycle.

3.2 Data sets

3.2.1 SMAP Level3 soil moisture for assimilation

Soil Moisture Active Passive (SMAP) is a satellite mission that follows a near-polar, sun-synchronous, 8-day repeat orbit (O'Neill et al., 2014). The L3SMP Level-3 soil moisture product is utilized in this study. It consists of daily estimates of global
115   soil moisture within the top ∼5 cm as retrieved by the SMAP passive microwave L-band radiometer (O'Neill et al., 2019). The soil moisture data are provided on a global, cylindrical 36 km Equal-Area Scalable Earth Grid, Version 2.0 (Brodzik et al., 2012) beginning from 31 March 2015.

L-band radiometry offers all-weather, diurnal sensing of the surface dielectric properties. The surface dielectric properties are a function of the near-surface soil moisture. Several mitigation features directed at preventing signal contamination due to
120   radio frequency interference (RFI) are built into the radiometer electronics and algorithms. Quality flags are included in the metadata to provide location specific details such as retrieval error, retrieval uncertainty, frozen ground conditions, presence of steep topography, and vegetation information (O'Neill et al., 2019).

3.2.2 In situ soil moisture measurements for model evaluation

Ground-based soil moisture measurements were obtained from the International Soil Moisture Network, an international,
125   multi-agency cooperation that provides global, in situ soil moisture measurements for the validation of model and remote sensing-based products (URL= https://ismn.earth/en/). Station measurements from four separate networks: 1) Ngari, 2) Naqu, 3) Maqu (Su et al., 2011; Zeng et al., 2016), and 4) CTP-SMTMN (Yang et al., 2013) were colocated with the land surface model grid for evaluation of the modeled estimates. The colocation was based on a simple arithmetic averaging of stations located within each grid cell.

130   The different networks represent varying local climates, although all networks are located at high elevations and have relatively cold climates. The Ngari network is located in an arid region, Naqu and CTP-SMTMN networks are situated in a semiarid region, and Maqu experiences a relatively humid climate, Fig. 1(a). The total number of stations available for evaluation is 101. Soil moisture measured at a depth of 5 cm below the surface was compared with model estimated surface soil moisture (soil layer depth = 0 to 5 cm). Measurements across the Tibetan Plateau are the only publicly available soil moisture measurements
135   within the study domain between the years 2015 to 2020.

3.2.3 ALEXI evapotranspiration for model evaluation

To study the influence of soil moisture assimilation on related geophysical fluxes, the Atmosphere-Land Exchange Inverse (ALEXI) evapotranspiration product was used. ALEXI estimates evapotranspiration (ET) using multi-sensor thermal infrared observations (Anderson et al., 2007, 2011). A two-source (soil and canpoy) land surface model is coupled to an atmospheric
140   boundary layer model in order to derive energy fluxes based on thermal imagery and insolation estimates derived from geostationary satellites. The thermal infrared information-driven surface energy balance model takes vegetation cover (obtained

from MODIS-based normalized difference vegetation index) and the change in radiometric temperature of the land surface as inputs and estimates sensible, latent and ground heat fluxes as well as evapotranspiration. The dataset version used in this study provides global ET estimates at 0.05° x 0.05° spatial resolution at a daily temporal scale.

3.2.4 FluxSat gross primary production for model evaluation

FluxSat is a satellite-based product that employs machine learning, reflectance data from Moderate-resolution Imaging Spectroradiometer (MODIS), and eddy covariance measurements to estimate global gross primary production (Joiner and Yoshida, 2020). Gross primary production (GPP) is an important variable within the carbon cycle. It represents the rate at which carbon is assimilated into the plant biomass per unit area per time during photosynthesis (Gough, 2011). GPP impacts the water cycle as plants transpire water during photosynthesis, thereby acting as moisture sources for the atmosphere and moisture sinks within the soil (Philander, 2008). FluxSat is developed by training neural networks using MODIS reflectance data to upscale GPP obtained from eddy covariance flux tower measurements (Joiner and Yoshida, 2020). FluxSat GPP was used here to study the influence of soil moisture assimilation on the carbon cycle.

3.2.5 GOME-2 fluorescence for model evaluation

In addition to GPP from FluxSat, solar-induced fluorescence (SIF) retrievals were also utilized to investigate the influence of soil moisture assimilation on the resulting carbon flux. Joiner et al. (2013) retrieved chlorophyll fluorescence using observations near the 740 nm emission peak gathered by the Global Ozone Monitoring Experiment 2 (GOME-2) spectrometer aboard the European meteorological (MetOp) satellites. Satellite-based fluorescence retrievals can be exploited to infer the functional status of vegetation (Van der Tol et al., 2014). Chlorophyll-excitation induced by solar energy results in fluorescence generated during photosynthesis. Carbon is then taken in by vegetation during photosynthesis. Considering the link to photosynthesis, Joiner et al. (2014) used SIF as an analog for GPP and highlighted the conformity within their phenologic responses. Joiner et al. (2014) also examined the seasonal cycles of modeled GPP in conjunction with GOME-2 fluorescence retrievals to track seasonal patterns in photosynthesis. The GOME-2 satellite fluorescence data is available at a spatial resolution of 0.5° x 0.5° at a monthly time scale and includes estimated errors on the order of 0.1–0.4 mW m^{-2} nm^{-1} sr^{-1}.

3.3 Experimental framework

Three types of model runs were implemented in LIS, Fig. 2. Details of each of the three types of model runs are provided below.

3.3.1 Nominal replicate (NR)

Noah-MP was run for five years from 1 January 2010 to 31 December 2014 using a single, nominal replicate (NR) to provide initial soil moisture conditions for the open loop and data assimilation runs (discussed further below). The NR simulation was
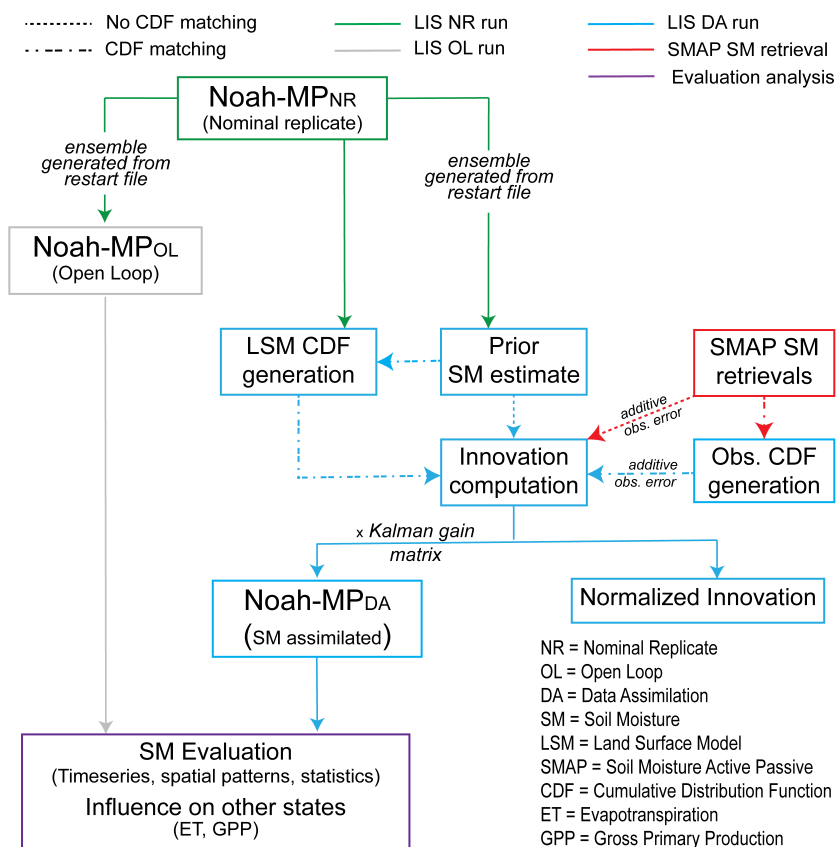
Figure 2. Overview of the soil moisture assimilation methodology implemented within the NASA Land Information System using the Ensemble Kalman Filter.

also utilized to develop the model cumulative distribution functions (CDFs) that were later used for CDF-matching during the assimilation run discussed in Sect. 3.3.3.

3.3.2 Open loop (OL)

The OL run represents a model-only run, i.e., the Noah-MP model was run in an ensemble configuration without any external
175 observations assimilated. The OL run serves as a baseline for Noah-MP's land surface modeling capability across South Asia for eventual comparison with the DA runs detailed in Sect. 3.3.3.

The NR restart file provided the initial conditions for the OL run which started on 1 January 2015 and extended to 30 September 2020 (Fig. 2). The NASA Land Data Toolkit (LDT; Arsenault et al. (2018)) was used to upscale to a 20-replicate ensemble from the single replicate NR restart file. The number of replicates was selected through an ensemble analysis. The
180 ensemble standard deviation (as a function of time) was studied as the number of replicates in the ensemble was increased from five to 50. It was found that as the number of replicates increased beyond 15, the ensemble standard deviation reached

an asymptotic value. Therefore, a 20-replicate ensemble was selected as an approximation of the probability distribution that reasonably represents the uncertainty in the model estimates.

185 Boundary conditions such as air temperature and radiative fluxes (i.e., incident shortwave and longwave radiation) were provided by the MERRA2 dataset. Boundary condition (forcing) perturbations used by Kwon et al. (2019) (Table 2) were applied while propagating the ensemble forward in time. Two different sets of precipitation datasets were used to drive Noah-MP: i) MERRA2 (Gelaro et al., 2017), and ii) GPM IMERG (Huffman et al., 2015). Usage of two different boundary condition (precipitation) sources was motivated by efforts to differentiate between the influence of model physics versus boundary conditions on the prognostic variables, e.g., soil moisture. Comparison of the results obtained from MERRA2-forced versus

190 IMERG-forced OL and DA experiments aided in understanding the influence of boundary conditions and the effect of SMAP retrieval assimilation on model SM estimation.

The OL simulation from 1 January 2015 to 30 September 2015 served as the model ensemble spin-up to achieve realistic uncertainty in soil moisture estimates. The results detailed in Sect. 4 are computed from the OL and DA experiments for water years 2016 to 2020. The water year demarcation used in this study starts in October of the preceding year (e.g., 2015) and ends

195 in September of the relevant year (e.g., 2016).

3.3.3 Data assimilation (DA)

SMAP SM retrievals are available from 31 March 2015 onwards. In accordance with the availability of SMAP retrievals, the DA run started on 1 April 2015 and extended to 30 September 2020. The ensemble Kalman filter (EnKF) assimilation algorithm was utilized to assimilate the SMAP SM retrievals into the Noah-MP modeled estimates.

200 The EnKF algorithm consists of two main steps: i) propagation step, and ii) update step. Noah-MP is the non-linear forward model used to propagate the prognostic state vector (y_t) forward in time as $y_t(x) = f(y_{t-1}(x), \alpha)$, where $f(\cdot)$ is the Noah-MP model, α is a vector of model parameters, t is time, and $x \in X$ defines the spatial domain. Equation (1) defines the formulation of the update step applied to the *a priori* state estimate (for each replicate) based on the difference between the model estimate and the observed value:

205
$$y_t^+(x) = y_t^-(x) + K_t(x)\,(z_t(x) + v_t - H(y_t^-(x)))$$
(1)

where $K_t(x) = C_{y_t z_t}(x)[C_{z_t z_t}(x) + C_{vv}]^{-1}$
(2)

such that $y_t^+(x)$ = *a posteriori* soil moisture value at time t, y_t^- = *a priori* soil moisture estimate at time t, $K_t(x)$ = Kalman gain at time t, $z_t(x)$ = SMAP soil moisture retrieval at time t, v_t = SMAP soil moisture retrieval error at time t such that

210 $v_t \sim \mathcal{N}(0, \sigma_{vv}^2)$, $H(.)$ is the linear observation operator, $C_{y_t z_t}(x)$ = time-varying cross-covariance matrix between the *a priori* state errors and the predicted observation errors, $C_{z_t z_t}(x)$ = time-varying predicted observation error covariance, and C_{vv} = time-invariant SMAP soil moisture retrieval error covariance.

The difference between the observation (plus observation error) and the mapped *a priori* model state estimate is known as the innovation, In_t. The normalized innovation (NI_t) is an effective diagnostic tool that aids in the diagnosis of the assimilation

215 framework and the origin of biases (Buehner, 2010). Equation (3) provides the normalized innovation formula for each replicate as:

$$NI_t(x) = \frac{z_t(x) + v_t - H(y_t^-(x))}{\sqrt{C_{z_t z_t}(x) + C_{vv}}} \tag{3}$$

The numerator in Eq. (3) equals In_t which is then normalized by the squared-root of the sum of $C_{z_t z_t}$ and C_{vv}. In an optimal DA system, the normalized innovations should exhibit a standard normal distribution ($NI_t \sim \mathcal{N}(0,1)$). To compute $C_{z_t z_t}$ and

220 C_{vv}, the prognostic state and observation error standard deviation was taken equal to 0.04 m^3 m^{-3} (O'Neill et al., 2014). It is worth noting here that the EnKF is expected to behave suboptimally given the nonlinearity of the Noah-MP model in conjunction with the non-Gaussianity of the SMAP retrieval errors. However, the exploration of NI_t sequence is a worthwhile exercise in an effort to better diagnose the behavior of the assimilation framework used in this study.

As part of the experimental matrix, the DA experiments were implemented using two different approaches. First, a CDF-

225 matching technique (Reichle and Koster, 2004) was used for bias correction of the SMAP soil moisture retrievals, herein referred to as DA-CDF. Monthly CDFs of the SMAP soil moisture retrievals and the Noah-MP modeled SM were developed using the NASA Land Data Toolkit. The monthly CDFs were then used to map the SMAP SM retrievals into the Noah-MP modeled soil moisture space prior to assimilation. The second approach employed no bias correction applied to the SMAP SM retrievals using CDF-matching and the *raw* SMAP SM was assimilated into Noah-MP, herein referred to as DA-NoCDF. The

230 relative systematic errors between SMAP SM and modeled Noah-MP SM are ignored during DA-NoCDF runs. The OL and DA runs were then compared against the evaluation datasets to analyze the influence of SM assimilation on the modeled states in Sect. 4.

4 Experimental results

Model estimates for water years (October to September) 2016 to 2020 are used to compute the results presented in this sec-

235 tion. Water years were used rather than Julian years due to the former's hydrologic suitability for the state variable under consideration, i.e., soil moisture (SM).

4.1 Evaluation using in situ measurements

In situ SM measurements available across the Tibetan Plateau were used to evaluate the modeled SM estimates. In situ measurements were collected at the point-scale whereas the Noah-MP grid size equaled 0.05° x 0.05° (~5.5 km x 5 km at mid-

240 latitudes). Some grid cells contain multiple stations located within the 0.05° x 0.05° area. If more than one station was located within a single grid cell, an average of the station measurements was used for comparison against the modeled SM estimates. Therefore, the total number of grid cells suitable for evaluation equaled 78 based on a total of 101 stations.

4.1.1 Timeseries evaluation

Figure 3 presents the OL, DA-CDF (i.e., CDF-matched), and DA-NoCDF (i.e., no CDF-matching) estimated SM timeseries
245 and their comparison with the in situ measurements at two grid cells from two different networks. These example sites were
selected because they reflect the performance of SM assimilation across two different climate zones. The Ngari network test
site (Figs. 3(a) and 3(b)) represents a cold and arid climate while the the Maqu network test site (Figs. 3(c) and 3(d)) is located
in a cold and humid climate.

For the Ngari network test site, MERRA2 forced modeled estimates overestimate the SM for all model simulations, Fig.
250 3(a). For MERRA2, the DA-NoCDF run has the lowest RMSE while the DA-CDF run shows the highest RMSE. In addition,
DA-NoCDF captures the measured values within the mean $\pm$ standard deviation ($\mu \pm \sigma$) range after 8 September 2016 while
the CDF-matched SMAP retrievals move the DA value in the opposite direction to the in situ measurements. MERRA2-forced
simulations exhibit improved consistency as the SM magnitude decreases with the approaching winter months. IMERG exhibits
much better temporal consistency with the measurements throughout the study period shown in Fig. 3(b). For IMERG, the DA-
255 CDF run has the lowest RMSE while the DA-NoCDF run has the highest RMSE. However, even the largest RMSE difference
(DA-CDF versus DA-NoCDF) is less than 0.004 m^3 m^{-3} indicating the limited influence of assimilation at this location. The
modeled values show localized underestimation as well as overestimation during different periods in the timeseries. For the
cold and arid test site, IMERG exhibits lower RMSE as compared to the MERRA2 boundary condition estimates, Figs. 3(a)
and 3(b).

260 Figures 3(c) and 3(d) present the Maqu test site timeseries for the MERRA2 forced and IMERG forced simulation runs,
respectively. The MERRA2 runs display better temporal consistency with the measurements as compared to the IMERG runs.
In Fig. 3(c), the DA-NoCDF run exhibits the lowest RMSE while the OL run has the highest RMSE magnitude. However,
the differences between the RMSE magnitudes for the different MERRA2 runs are minimal (i.e., less than 0.002 m^3 m^{-3}). In
Fig. 3(d), for IMERG the lowest RMSE is computed for the DA-NoCDF run while the OL has the highest RMSE magnitude
265 as well. However, the difference in the RMSE magnitudes is higher than the values in Fig. 3(c). There is a negative bias
(underestimation) apparent in all the IMERG runs after 1 August 2018. For the cold and humid test site, MERRA2 displays
better performance as compared to the IMERG boundary condition estimates, Figs. 3(c) and 3(d).

Figure 3 shows the presence of biases in the modeled estimates and SMAP SM retrievals with respect to the in situ measure-
ments. Relative to MERRA2, IMERG-based SM estimates have lower RMSE for both locations, indicating the importance of
270 precipitation boundary conditions in terms of SM estimation. The magnitude of state update for DA-NoCDF is generally larger
than DA-CDF. However, the magnitude of the update increments is limited by the model parameters (such as wilting point and
maximum SM capacity) and model and retrieval error assumptions (via ensemble uncertainty).

4.1.2 Statistical analysis

Relevant statistics were computed using all the measurements (from all the networks) available from October 2015 to Septem-
275 ber 2020 in conjunction with the corresponding Noah-MP modeled estimates. Table 2 presents mean bias, RMSE, unbiased
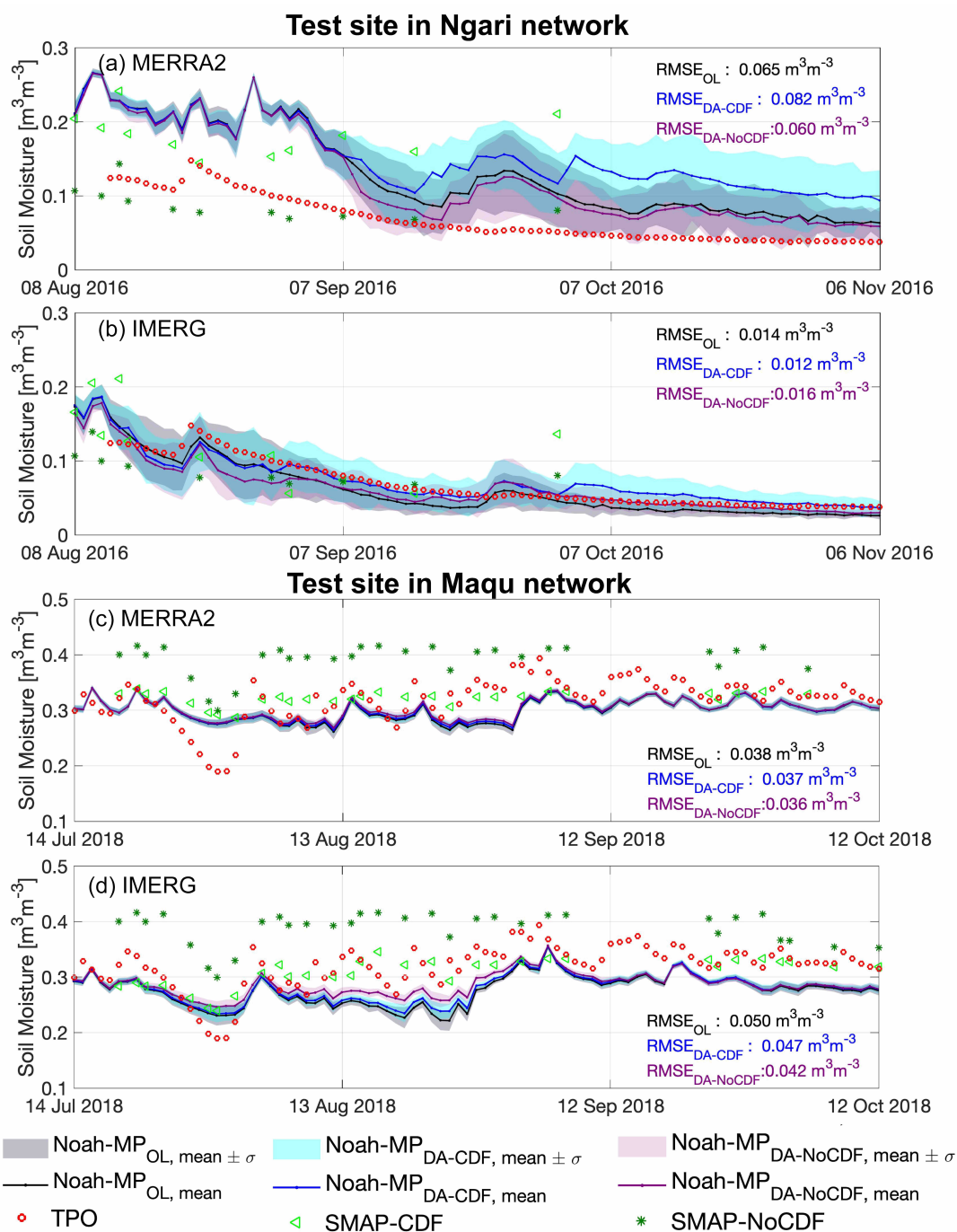
Figure 3. Comparative timeseries of OL and DA estimated surface (top 5 cm) soil moisture. The solid line represents the ensemble mean whereas the shaded areas represent ± 1 standard deviation (σ) across the full ensemble.

Table 2. Statistics of OL and DA soil moisture estimates (2015 to 2020) computed with respect to the soil moisture measurements across the Tibetan Plateau. All values are in units of m^3 m^{-3} unless otherwise indicated. Mean refers to the average of all the stations included within the network. OL = Open Loop, DA-CDF = CDF-matched SMAP retrieval assimilation, and DA-NoCDF = data assimilated estimates without CDF matching of the SMAP retrievals.

Tibetan Plateau	MERRA2			IMERG		
Statistic	**OL**	**DA-CDF**	**DA-NoCDF**	**OL**	**DA-CDF**	**DA-NoCDF**
Mean bias	0.070	0.070	0.059	0.031	0.033	0.025
Confidence interval$_{95\%}$ limits- bias	0.012	0.012	0.012	0.011	0.011	0.011
Mean RMSE	0.130	0.130	0.122	0.106	0.106	0.100
Confidence interval$_{95\%}$ limits- RMSE	0.007	0.007	0.008	0.008	0.008	0.008
Mean unbiased RMSE	0.066	0.066	0.060	0.066	0.064	0.061
Confidence interval$_{95\%}$ limits- unbiased RMSE	0.004	0.004	0.003	0.004	0.004	0.004
Median relative RMSE [-]	1.873	1.873	1.794	1.507	1.507	1.480
Mean R	0.295	0.300	0.370	0.327	0.321	0.447

RMSE, and correlation (R) computed for the OL, DA-CDF, and DA-NoCDF estimated SM. The individual statistics were calculated for each grid cell separately and were then averaged to represent the domain-averaged statistical performance of the modeled SM. The total number of grid cells used for comparison is equal to 78. A majority of the Ngari, Naqu, and CTP-SMTMN network stations are situated at locations where SMAP L3 retrievals have limited availability (Figs. 1(a) and 7(f)). These high elevation locations are completely frozen or partially frozen during a considerable part of the year leading to limitations in the applicability of the tau-omega algorithm used to retrieve soil moisture information from the SMAP observed brightness temperatures (O'Neill et al., 2014). Given that little or no assimilation occurs over several stations, several of the statistics computed for the OL, DA-CDF, and DA-NoCDF estimated soil moisture are quite similar.

MERRA2 and IMERG exhibit similar relative results, i.e., the lowest mean bias, RMSE, unbiased RMSE, and relative RMSE is computed for the DA-NoCDF run. Similarly, the highest correlation is also observed for the DA-NoCDF run. For MERRA2, in terms of mean bias the OL/DA-CDF and DA-NoCDF intersect at the 95% confidence interval limit (0.070±0.012 m^3 m^{-3} versus 0.059±0.012 m^3 m^{-3}). Similar values are computed for RMSE (0.130±0.007 m^3 m^{-3} versus 0.122±0.008 m^3 m^{-3}) and unbiased RMSE (0.066±0.004 m^3 m^{-3} versus 0.060±0.003 m^3 m^{-3}). The IMERG mean bias, RMSE, and unbiased RMSE, however, overlap within the 95% confidence interval limits (columns 5-7 in Table 2).

Relative RMSE is calculated as the ratio of the RMSE to the standard deviation of the state variable (SM). The median relative RMSE highlights the relative accuracy of the majority of the grid cells. A relative RMSE of less than 0.7 indicates medium or high goodness-of-fit depending on the state variable (McCuen, 2016). In terms of comparative values, the DA-NoCDF runs for both MERRA2 and IMERG show lower median relative RMSE magnitudes than the OL and DA-CDF estimates. Overall,
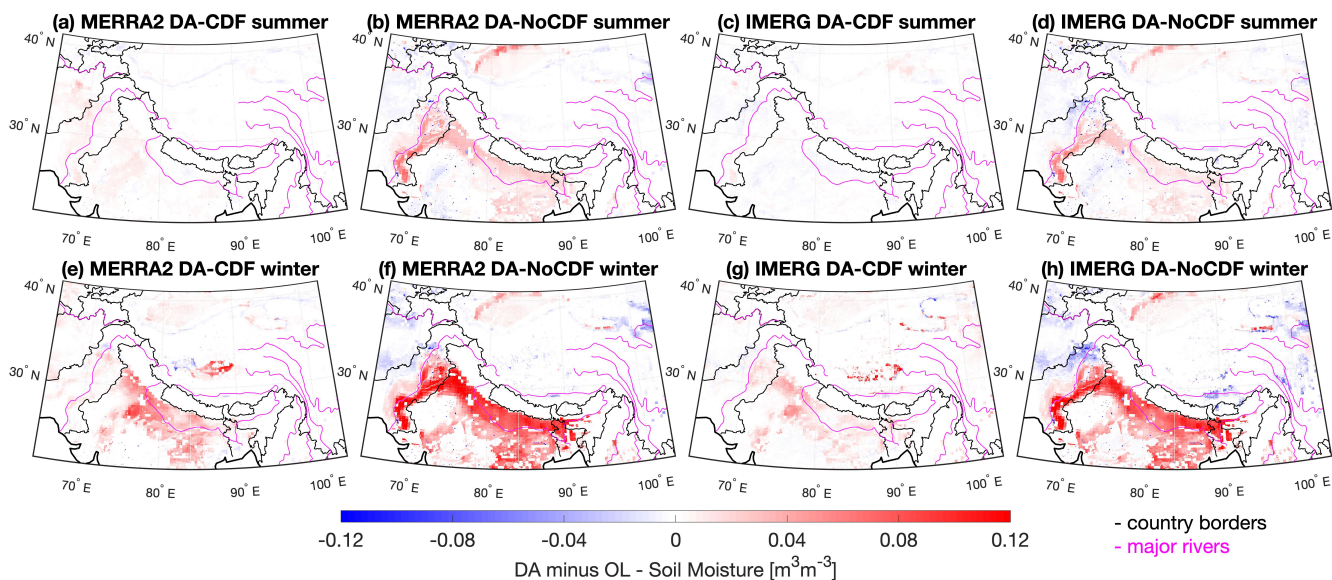
Figure 4. Differences between the mean soil moisture estimated by the OL and DA simulations during the summer (April 2016 to September 2016) versus the winter months (October 2015 to March 2016) highlight: i) the unmodeled irrigation signal across croplands, and ii) the relatively higher influence of assimilation on soil moisture estimates during the winter period as compared to the summer period. DA-CDF= assimilation of CDF-matched SMAP retrievals and DA-NoCDF= no CDF-matching of SMAP retrievals.

it is observed that the IMERG statistical values are lower than the corresponding MERRA2 values, thereby indicating better performance of the IMERG-forced model estimates as compared to MERRA2 across the Tibetan Plateau.

4.2 Spatial analysis of OL versus DA

Figure 4 shows the difference in spatial patterns of the SM estimated by the OL and the DA-CDF/DA-NoCDF simulations during the summer (April to September) and winter (October to March) months. This temporal grouping is motivated by the precipitation climatology (i.e., summer monsoon versus winter westerlies) of the region (Dhar and Nandargi, 2003), which also influences the irrigation patterns in the region. Two main crop seasons are noted across South Asia, i.e., the summer (Kharif) crop and the winter (Rabi) crop (Biemans et al., 2016). Precipitation, snowmelt, and ground water extraction are the main sources of river runoff that provides water for irrigation (Armstrong et al., 2018).

The magnitudes of DA minus OL values shown in the summer maps are relatively lower than the magnitudes in the winter maps for all DA experiments. This feature suggests that there is a relatively higher consistency between the OL and DA-CDF/DA-NoCDF runs (i.e., smaller DA minus OL magnitudes) during the summer months when the bulk of the precipitation occurs, especially in the lower latitudes, as compared to the winter months. A spatial feature apparent in Figs. 4(b), 4(d), 4(f), and 4(h) is the occurrence of large differences in areas surrounding the major rivers in the lower latitudes ($\lesssim 31°$ N). The location of these large differences indicates the influence of irrigation on the water budget. Fig. 7(c) includes the map of the
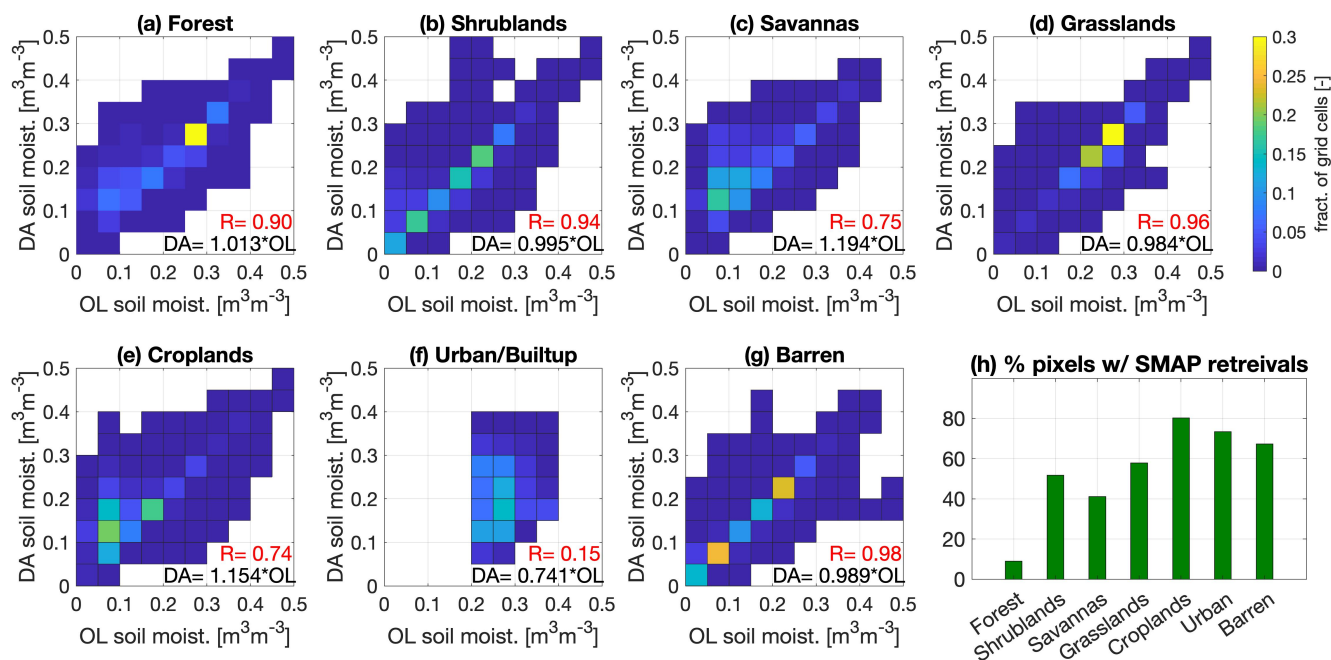
Figure 5. Comparison of OL versus DA-NoCDF estimated soil moisture according to the dominant landcover types present within the study domain. The OL and DA-NoCDF joint PDFs (presented here as fractions of grid cells) are computed from the LIS runs with MERRA2 boundary conditions during the winter months of WY 2016.

total percentage of irrigated area per grid cell that corresponds well with the cropland landcover type shown in Fig. 2(d). These
310 three maps highlight the increase in model estimated SM by the assimilation of raw (i.e., no CDF matching applied) SMAP retrievals in the irrigated cropland grid cells. Further, comparing the MERRA2 maps (Figs. 4(a), 4(b), 4(e), and 4(f)) with the IMERG maps (Figs. 4(c), 4(d), 4(g), and 4(h)) it appears that the influence of the boundary conditions used (MERRA2 versus IMERG) is damped by more dominant influencing factors such as anthropogenic irrigation and the seasonal precipitation pattern. In other words, similar spatial patterns in DA minus OL are visible in both the MERRA2 and IMERG forced model
315 estimates.

The DA-NoCDF simulation exhibits higher differences with the OL relative to the DA-CDF run. Therefore, to further dissect its spatial patterns with respect to landcover and soil texture, Figs. 5 and 6 were created. Fig. 5 presents the OL and MERRA2-forced DA-NoCDF joint PDFs (shown here as fractions of total landcover type grid cells) for the winter months of the 2016 water year. The bar graph in subplot 5(h) provides the percentage of grid cells for each landcover type that have at least one
320 instance of SMAP retrieval assimilation. The highest percentage is observed for grid cells belonging to the cropland type.

Linear regression coefficients included in all the subplots of Fig. 5 represent the slope between the two axes. If the slope is >1 then, in general, the variable on the y-axis (here DA-NoCDF) has greater soil moisture magnitudes than the x-axis (here OL). Forest (subplot 5(a)), savannas (subplot 5(c)), and cropland (subplot 5(e)) landcover types show >1 linear regression coef-

ficients, indicating that, in general, the SMAP assimilation increases the soil moisture magnitude across grid cells belonging to

325 these landcover types. Interesting to note is that the percentage of grid cells with assimilation is quite different for these three landcover types (forest=10%, savannas=40%, and cropland=80%). For shrublands (subplot 5(b)), grasslands (subplot 5(d)), urban/built-up (subplot 5(f)), and barren (subplot 5(g)) landcover types, the linear regression coefficients are <1 indicating that, in general, the SMAP assimilation decreases the soil moisture magnitude across grid cells belonging to these landcover types. The lowest regression coefficient is computed for the urban/built-up landcover type. The correlation coefficients for

330 savannas, croplands and urban/built-up are ≤0.75 and are relatively lower than the other landcover types, which suggests that SMAP SM assimilation alters the SM estimates across grid cells belonging to these three landcover types the most (Note: if the SM assimilation caused no change, the OL and DA SM estimates would be nearly identical, and hence the correlation coefficient between the two would equal 1.). The lowest correlation is computed for the urban/built-up landcover type, of which 70% of the grid cells underwent assimilation, however, this landcover type only represents 0.4% of the total domain grid cells

335 (Table A1). Similar results were observed for the IMERG-forced simulation as well (results not shown).

Figure 6 displays the OL and MERRA2-forced DA-NoCDF joint PDFs (shown here as fractions of total grid cells) categorized with respect to the soil texture types for the winter months of the 2016 water year. The bar graph in subplot 6(h) provides the percentage of grid cells belonging to each soil texture type that have at least one instance of SMAP retrieval assimilation. The soil types that included sand or loam exhibited regression coefficients >1 (except for loamy sand). Grid cells belonging

340 to loamy sand (subplot 6(b)), silty clay (subplot 6(h)), and clay (subplot 6(i)) soil types exhibited regression coefficients <1, indicating a general decrease in SM magnitude after SMAP assimilation. However, the regression coefficients of all three of these soil texture types are close to one, and therefore, do not reinforce any significant influence of SMAP assimilation on grid cells belonging to these particular soil texture types.

4.3 Irrigation impact

345 In South Asia, irrigation is implemented through routing of the: i) river runoff (contributed by snowmelt and precipitation), ii) discharge from storage reservoirs such as dams, and iii) water pumped from subsurface aquifers, using a network of canals and tube wells (Chambers, 1988). The GMIA total irrigation-equipped area map in Fig. 7(e) visualizes this practice as high magnitudes are observed in the areas surrounding the major rivers in Pakistan, India, and Bangladesh.

Irrigation is not explicitly modeled in the Noah-MP land surface modeling environment. Therefore, to investigate the effect

350 of SM assimilation on irrigated areas in further detail, the maps of temporal mean normalized innovation (NI) were compared against the GMIA total irrigation-equipped area map. NI (detail in Sect. 3.3.3) represents the difference between the observations (i.e., SMAP SM retrievals) and the modeled *a priori* estimates. A positive NI value indicates that the *a priori* state estimate is less than the observed value while a negative NI value indicates that the *a priori* state estimate is greater than the observed value. For an unbiased, optimal assimilation framework, the NI sequence exhibits a mean of 0 and a standard

355 deviation equal to 1 over time. Therefore, high positive or negative NI values reveal the presence of bias either in the model estimates or the assimilated retrievals.
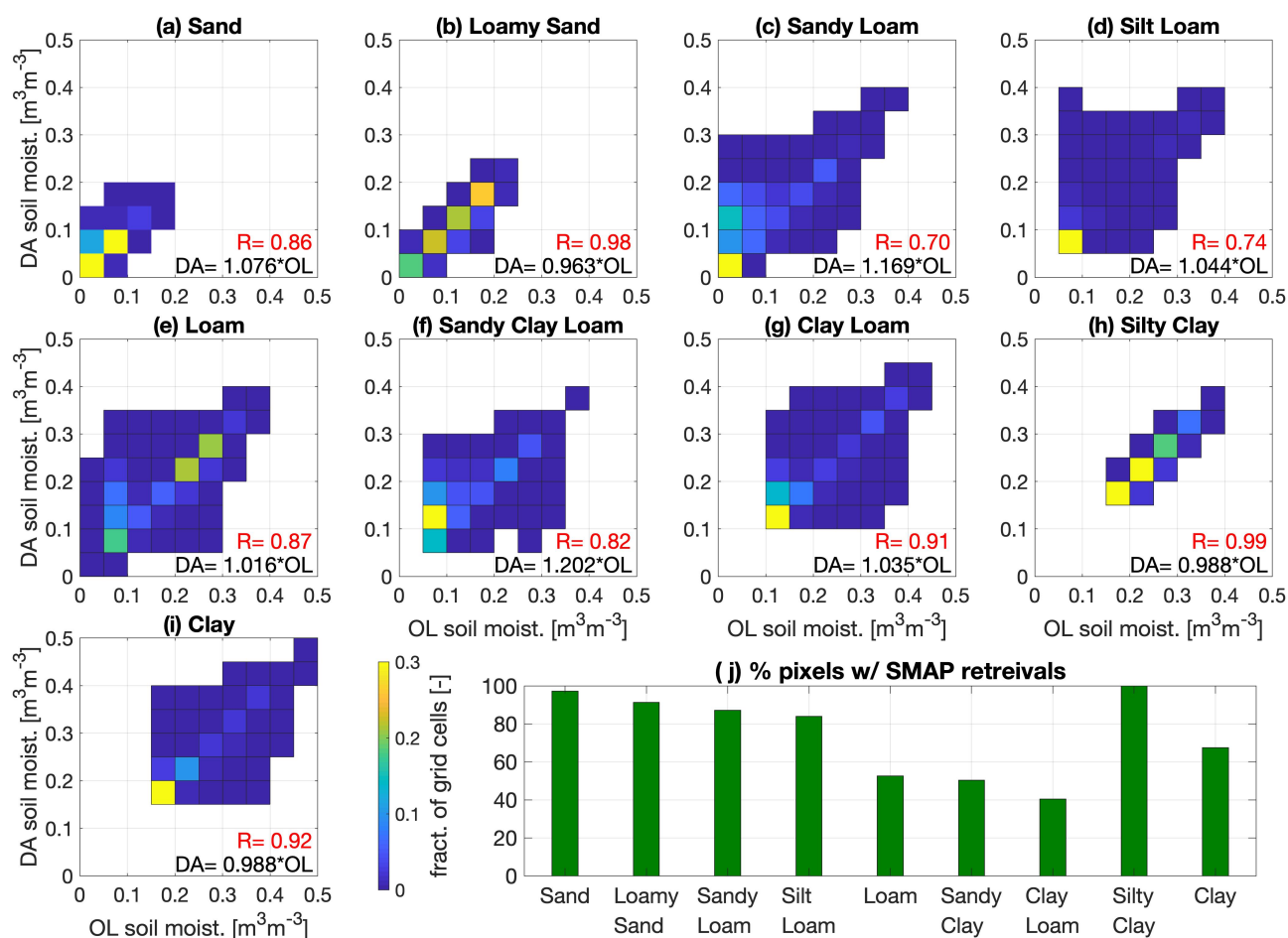
Figure 6. Comparison of OL versus DA-NoCDF estimated soil moisture according to the dominant soil texture types present within the study domain. The OL and DA-NoCDF joint PDFs (presented here as fractions of grid cells) are computed from the LIS runs with MERRA2 boundary conditions during the winter months of WY 2016.
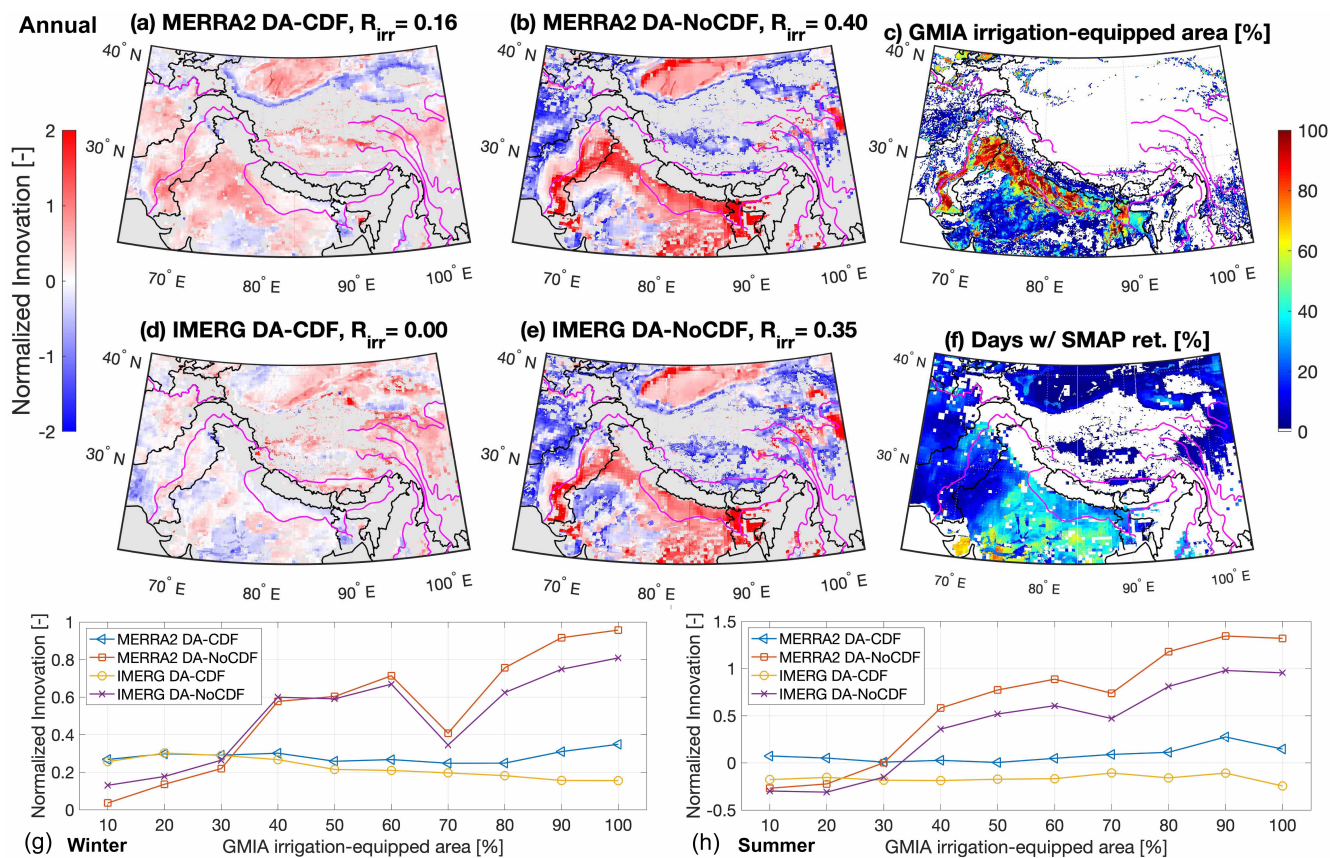
Figure 7. The spatial patterns in normalized innovation (NI) maps present the results of CDF-matched (DA-CDF) versus raw SMAP SM retrievals (DA-NoCDF), subplots (a), (b), (d), and (e). Grey areas represent grid cells where no assimilation occurred due to missing SMAP SM retrievals. The improved spatial correlation with respect to irrigation-equipped area (R_{irr}) for both of the DA-NoCDF maps (subplots (c) and (d)) highlights the correction of SM biases due to an unmodeled hydrologic process, i.e., irrigation. Subplots (g) and (h) underscore the increase in NI magnitude for both DA-NoCDF (MERRA2 and IMERG) simulations as the total irrigation-equipped area increases for summer and winter months, respectively. Subplot (c) presents the total percentage of irrigated area per grid cell developed from the Global Map of Irrigated Areas (GMIA) dataset provided by the Food and Agriculture Organization. Subplot (f) shows the % of total days in the study period on which SMAP retrievals were assimilated.

A number of distinct features can be observed in the NI maps presented in Fig. 7. MERRA2 DA-CDF and DA-NoCDF, and IMERG DA-NoCDF spatial patterns show positive NI values in Pakistan (Indus Basin) and the areas surrounding the Ganges River in India, Figs. 7(a), 7(b), and 7(e). Comparing the location of these positive NIs with the GMIA total irrigation-equipped

360   area map (Fig. 7(c)), it is apparent that the SMAP retrievals have higher SM magnitudes across irrigated areas. SMAP retrievals implicitly contain the effects of irrigation and subsequently transfer that information to the modeled estimates via assimilation. Hence, the water budget across these locations was corrected as information related to an unmodeled soil moisture source was effectively incorporated into the land surface model. Figures 7(g) and 7(h) show the general increase in mean NI magnitudes during the winter and summer months, respectively, as the percentage of irrigation-equipped area increases. NIs computed

365   from the MERRA2 and IMERG DA-CDF runs, however, do not display this pattern.

     Further comparing the MERRA2 and IMERG DA-NoCDF NI maps with the water storage trends identified by Fig. 1 in Girotto et al. (2017) and Fig. 2 in Loomis et al. (2019), the locations in the northwestern part of India that show negative water storage trends (resulting from groundwater pumping for purposes of irrigation) are spatially consistent with high positive NI values. The additional water introduced into the hydrologic cycle via pumping from subsurface aquifers is captured by the

370   SMAP SM retrievals and is then used to condition the modeled estimates via assimilation.

     The spatial patterns in NI show different magnitudes (and even different signs) at some locations for DA-CDF versus DA-NoCDF. The visible difference in NI signs is due to the implementation of CDF matching of the assimilated retrievals during the DA-CDF simulation. If the model estimates are biased, traditional data assimilation generally does not result in optimal estimates (Zhang and Moore, 2015). Mapping the observation CDF to a biased model CDF would ultimately transfer the model

375   bias into the CDF-matched observations. Therefore, in cases where the model estimates are inherently biased, assimilation of CDF-matched retrievals could update the *a priori* state estimates in the wrong direction. This phenomenon is apparent in IMERG DA-CDF versus IMERG DA-NoCDF NI maps across the irrigated areas and the Tibetan Plateau.

     One interesting pattern to note is the presence of highly negative NI values across the high elevation areas (Hindukush mountains) in the western part of the domain in the DA-NoCDF maps (subplots 7(b) and 7(e)). Comparing the DA-NoCDF

380   NI maps with the DA minus OL map in Fig. 4, it is apparent that the high NI values did not manifest into high DA minus OL values. A high NI magnitude does not necessarily lead to a subsequently high update. If the model state error variance is quite low, the denominator in Eq. 3 will be a small value that can then result in a large NI if the nominator (innovation) is relatively large. However, a low model state error variance results in a reduced Kalman gain (due to $C_{y_t z_t}$), and hence, the computed update will be relatively small.

385   High NI magnitudes are observed in the Indus Basin even though assimilation occurred during $<20\%$ of the total days (in the study period) at these locations. This suggests that the quantitative effect of SMAP SM retrieval assimilation is not primarily based on the assimilation frequency, but rather the large differences between the SMAP and *a prioi* estimates. The DA-CDF versus DA-NoCDF results seen here are similar to the experiments conducted by Kumar et al. (2015) to evaluate SM retrievals across irrigated areas. Their study showed that bias correction of observations via CDF matching can lead to the removal of the

390   information pertaining to the unmodeled processes from the observations when the estimation bias stems from the absence of such processes in the model.
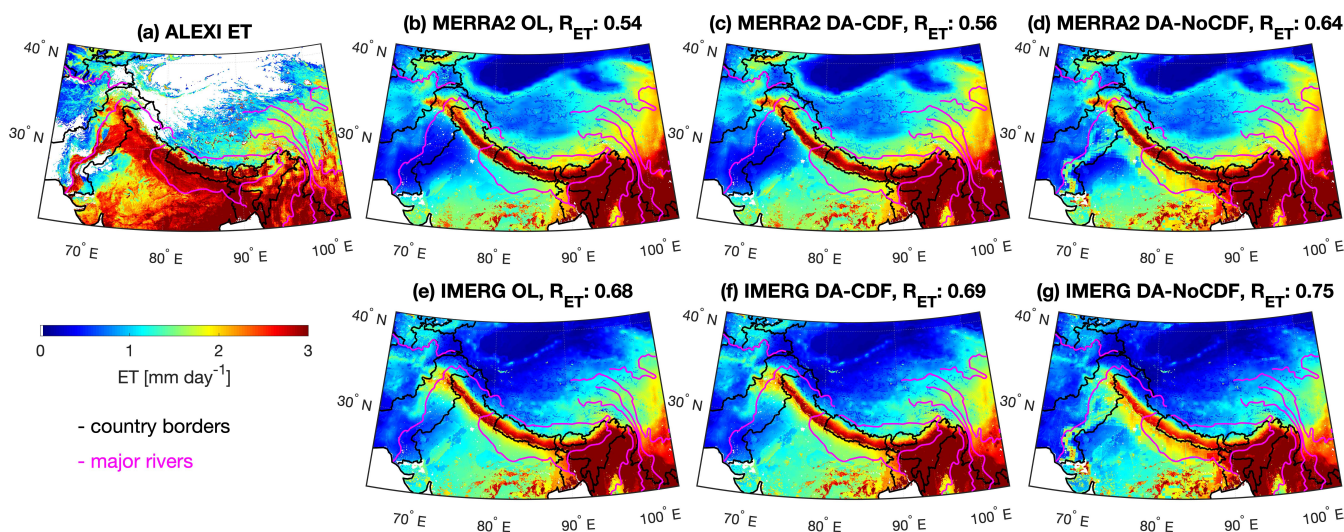
Figure 8. Comparative maps of modeled evapotranspiration (ET) with respect to the ALEXI evapotranspiration estimates (Sect. 3.2.3) for WY 2016. DA-NoCDF maps show relatively higher spatial consistency with ALEXI ET, particularly in areas surrounding the major rivers in lower latitudes ($<30°$). The correlation values (R_{ET}) indicate the spatial consistency between annual mean ET estimated by ALEXI and the corresponding Noah-MP simulation.

4.4 Influence on water and carbon cycle

SM is an important component of the water cycle. It is, therefore, expected that changes in the SM estimates would translate into changes in hydrologic variables that are dependent on SM such as evapotranspiration (ET). ET is composed of evaporation
395 from the soil and vegetation as well as transpiration from the vegetation. While ET is used to represent the water cycle in this section, gross primary production (GPP) and solar-induced chlorophyll fluorescence (SIF) are utilized as vegetation proxies that represent the carbon cycle.

In order to diagnose the influence of SMAP SM assimilation on ET, the mean annual ET from the MERRA2 and IMERG-forced OL, DA-CDF, DA-NoCDF simulations is analyzed. Figure 8 highlights the improved spatial consistency (relative to the
400 ALEXI ET) of the DA-NoCDF estimates (subplots 8(d) and 8(g)) compared to the OL (subplots 8(b) and 8(e)) and DA-CDF ET (subplots 8(c) and 8(f)). The spatial correlation of mean annual ET calculated with respect to the ALEXI ET for the MERRA2 runs increases from 0.54 for the OL to 0.56 for DA-CDF and 0.64 for the DA-NoCDF estimates. Similarly, there is an increase in the spatial correlation of the IMERG runs from 0.68 for the OL to 0.69 and 0.75 for the DA-CDF and DA-NoCDF estimates, respectively. The DA-NoCDF estimates for both sets of boundary conditions show relatively higher spatial correlation with the
405 ALEXI ET, particularly in the Indus River Basin, where surface irrigation is significant. All three of the MERRA2 estimates show higher ET magnitudes across the Tibetan Plateau as compared to the IMERG runs, which corresponds well with the higher positive bias computed in MERRA2-forced SM estimates (see Table 2). All of the IMERG simulations exhibit better overall spatial correlation with ALEXI ET relative to the MERRA2 runs.

low
10.5194/hess-2021-460
2021-09-08
Hydrology and Earth System Sciences
journal article
en
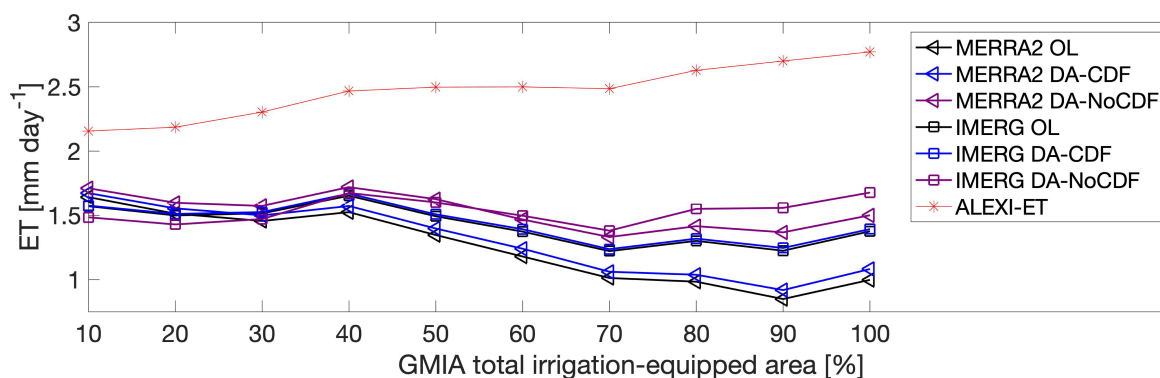
Figure 9. The magnitude of average evapotranspiration (ET) increased as the percentage of irrigated area within the grid cell increased. OL= Open Loop, DA-CDF= CDF-matched SMAP retrieval assimilation, and DA-NoCDF= data assimilated estimates without CDF matching of the SMAP retrievals. ALEXI ET provides independent ET estimates for evaluation of the Noah-MP modeled ET.

Comparing the spatial patterns in ET magnitudes with the GMIA irrigation-equipped area map (Fig. 7(c)), it can be seen

410 that the mean ET magnitudes across irrigated areas, particularly across the Indus basin, increased for DA-NoCDF simulations (Figs. 8(d) and 8(g)) relative to the OL. However, this feature is absent in the DA-CDF simulations (Figs. 8(c) and 8(f)). The spatial patterns observed in the DA minus OL SM (see Figs. 4(f) and 4(h)) are similarly shown in the ET maps (Figs. 8(d) and 8(g)) in terms of higher ET magnitudes observed for grid cells belonging to the cropland landcover type.

Further investigation of this feature highlighted the correction of SM and ET in irrigated areas via SMAP assimilation. It

415 is expected that as the irrigation percentage increases the surface SM would also increase. The increase in SM, in general, translates into an increase in ET. Figure 9 shows the increase in ALEXI ET as the percentage of irrigated area (Fig. 7(c)) in each grid cell increases. In contrast, the OL and DA-CDF estimates do not capture this behavior, and alternatively, show declining ET values for regions with 40% or more total irrigation-equipped area when using the MERRA2 boundary conditions. The IMERG OL and DA-CDF estimates show approximately the same decreasing trend. However, the DA-NoCDF estimates

420 corrected the decreasing magnitudes for grid cells with >40% total irrigation-equipped area for both sets of precipitation boundary conditions.

The ALEXI ET dataset serves as an independent evaluation source for OL, DA-CDF, and DA-NoCDF ET estimates. The ET magnitudes for all the modeled runs are lower than the ALEXI ET, which could be attributed to the absence of relevant processes (e.g., surface irrigation) in Noah-MP, whereas the ALEXI product implicitly includes this information. Although

425 ALEXI is a modeled dataset, it is based on remote sensing data and has been shown to detect irrigation (Knipper et al., 2019). These results suggest assimilation of SMAP SM retrievals in the absence of CDF-matching can help correct for some of the missing physics in the Noah-MP land surface model.

Figures 10(a), (b), and (c) were created to further dissect the influence of SMAP assimilation on the water and carbon cycle over irrigated regions. The test site selected contains 88% total irrigation-equipped area and belongs to the cropland landcover
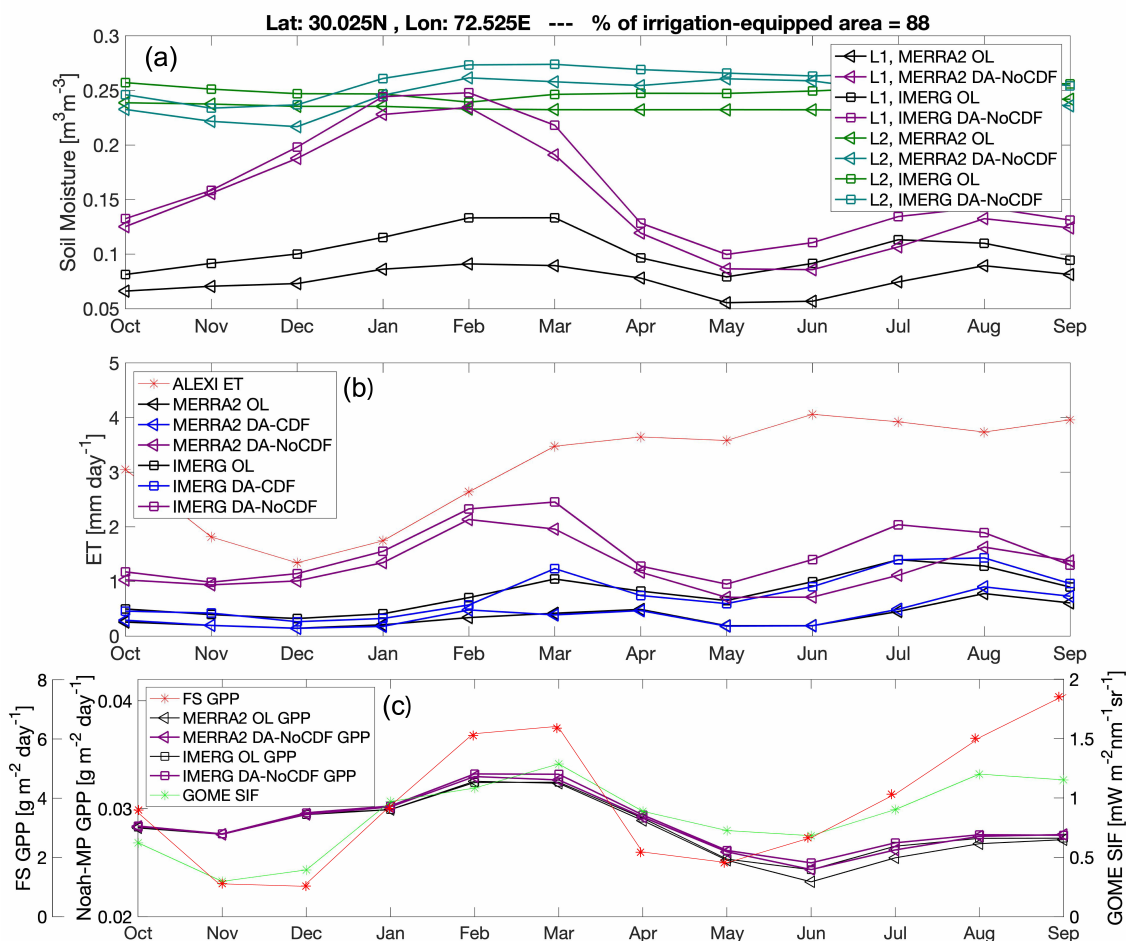
Figure 10. Influence of SMAP soil moisture (SM) assimilation on an irrigated location is assessed through soil moisture of successive soil layers (L1 and L2), evapotranspiration (ET) and the corresponding behavior of the dynamic vegetation (represented by the gross primary production (GPP)). ALEXI ET (Sect. 3.2.3) and GOME solar-induced chlorophyll fluorescence (SIF) (Sect. 3.2.5) are used as evaluation datasets. (a) L1 = layer 1 near-surface SM and L2 = layer 2 root-zone SM. Noah-MP modeled ET exhibits similar temporal patterns as the near-surface SM (L1); however, root-zone (L2) SM and GPP are not correspondingly modulated.

430   type. Noah-MP divides the soil profile into four layers. Figure 10(a) shows the monthly temporal variation in near-surface (first soil layer, L1) and root-zone (second soil layer, L2) soil moisture (SM) at this location. The first (top) soil layer (L1) is 5 cm deep, while the second layer (L2) extends 35 cm below that. L1 estimates for all simulations exhibit a seasonal variation in the surface SM with the major peak occurring in Feb and a minor local peak in Aug. The DA-NoCDF runs for both sets of boundary conditions depict a higher seasonal amplitude as compared to the OL. Comparing the L1 values with the L2 values,

435   the damping of the seasonal variation amplitude is apparent in L2, i.e., the influence of assimilation on surface SM is not proportionally translated into the root-zone SM. However, compared to the OL, the DA-NoCDF estimates for L2 do exhibit seasonal variation (albeit to a limited extent). The DA-CDF estimates were quite similar to the OL L1 and L2 estimates and are thus excluded from the graph for visual clarity. Figure 10(b) highlights the translation of L1 SM temporal patterns into ET estimates. ALEXI ET displays much higher magnitudes of ET throughout the year. The DA-NoCDF simulations exhibit better

440   consistency with ALEXI ET as compared to the OL and DA-CDF ET for both sets of precipitation boundary conditions.

    Figure 10(c) presents the impact of SM on vegetation in terms of gross primary production (GPP) and solar-induced fluorescence (SIF). Compared to the FluxSat GPP (Sect. 3.2.4), the magnitude of OL and DA (Noah-MP) GPP observed at this location is relatively small. However, similar seasonal variability (not magnitude) is observed in all the Noah-MP simulations similar to the FluxSat GPP (peaks in Feb/Mar and Aug/Sep). The OL, DA-CDF (not shown in figure), and DA-NoCDF GPP

445   estimates exhibit high similarity and do not differ significantly throughout the year. A possible explanation for this behaviour is that vegetation transpiration is more dependent on root-zone SM than surface SM. In Fig. 10(b), it is seen that the change in near-surface (L1) SM is largely modulated in terms of root-zone (L2) SM. In general, root-zone SM tends to maintain low variation throughout the year. Thus, it is expected that assimilation of surface SM retrievals may not significantly impact the dynamic vegetation.

450   FluxSat GPP and Noah-MP GPP were compared with respect to dominant landcover types and it was observed that the SMAP assimilation did not influence the vegetation within any of the landcover type grid cells to a high extent, Fig. 11. Even the highest percent improvement in the RMSE, computed for savannas (normalized information content (NIC) = 4.5%, see Appendix B for formula) during the summer months was <5%. The correlations between GOME-SIF and the different Noah-MP modeled estimates are similar in magnitude and do not highlight any significant influence of SMAP assimilation (OL

455   versus DA-NoCDF) with respect to individual landcover types. Comparing these results to the vegetation optical depth (VOD) assimilation implemented by Kumar et al. (2020), it seems that the modeled GPP estimates are relatively more improved by assimilating VOD than surface SM. In the context of land surface modeling with Noah-MP, surface SM exhibits a weaker influence on GPP as compared to VOD. This is because SM has an indirect effect on GPP, whereas assimilation of VOD has a direct impact on plant biomass, and hence, on GPP. Kumar et al. (2020) found that SM had a higher control over ET and GPP

460   during moisture-limited conditions.
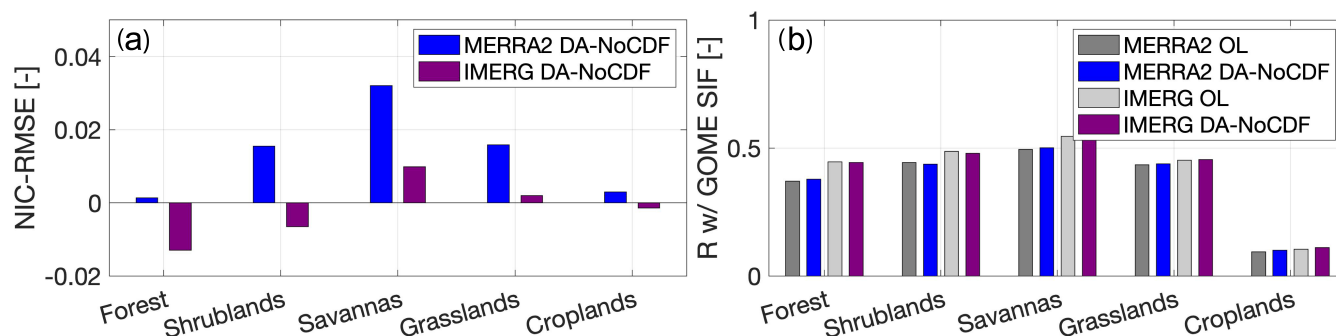
Figure 11. (a) Normalized information content (NIC) with respect to RMSE ($RMSE_{OL}$ versus $RMSE_{DA-NoCDF}$) is computed through comparison with FluxSat gross primary production (GPP). All landcover types exhibit low NIC_{RMSE} magnitudes (<0.1). (b) Correlation with GOME solar-induced chlorophyll fluorescence (SIF) depicts the spatiotemporal consistency between the Noah-MP modeled GPP and GOME SIF. R values for the OL versus DA-NoCDF GPP estimates for all landcover types are quite similar. Data from the summer months of WYs 2016-2019 were used to compute the metrics.

5 Conclusions

Soil moisture estimation across South Asia was implemented in this study by assimilating SMAP soil moisture retrievals into a land surface model. The Noah-MP land surface model was run within the NASA Land Information System software framework to simulate the regional land surface processes. Precipitation boundary conditions (in different experiments) were provided by the NASA Modern-Era Retrospective Analysis for Research and Applications (MERRA2) and GPM Integrated Multi-satellite Retrievals (IMERG) products. SMAP retrieval assimilation was implemented using two approaches: i) DA-CDF= mapping of the SMAP retrieval CDF to the land surface model climatology prior to assimilation, and ii) DA-NoCDF = SMAP retrieval assimilation without CDF-matching. CDF-matching of the observations to the modeled estimates was applied in an effort to correct the distribution moments of the SMAP soil moisture retrievals.

Comparison of assimilated and model-only soil moisture estimates against in situ measurements showed the relative improvement in soil moisture by assimilating SMAP retrievals. The IMERG DA-NoCDF simulation exhibited the best goodness-of-fit and reduced the mean bias and RMSE by 8.4% and 9.4% across the Tibetan Plateau. The results presented in Sect. 4 highlight that SMAP assimilation decreased the magnitude of error (Table 2), and improved the spatiotemporal soil moisture patterns (Figs. 3 and 7) and associated evapotranspiration (Fig. 8), particularly over irrigated areas. However, the influence on evapotranspiration did not proportionally translate into changes in the carbon flux.

The most important feature of SMAP retrieval assimilation observed in this study is the correction of state estimation biases generating from missing physics in the land surface model (unmodeled hydrologic process), i.e., irrigation. Information about the exact quantity and timing of irrigation practices is generally not publicly available except for a few parts across the globe. The framework described in this paper could possibly be used to infer information regarding irrigation patterns and practices using an inverse method.

The utility of L-band radiometry for soil moisture estimation is limited by the soil penetration depth associated with PMW (∼5 cm) and the data gaps in the soil moisture retrievals. These data gaps are due to the presence of snow, ice, frozen soil, dense vegetation, and RFI instances. Therefore, the influence of SMAP soil moisture retrieval assimilation was primarily limited to surface soil moisture, compared to root-zone soil moisture, across locations where SMAP soil moisture retrievals

485 where available for assimilation. However, improvements in the fine-scale spatial and temporal patterns in soil moisture were observed even though the retrievals being assimilated were at a much coarser scale than the model grid (36 km versus 0.05°). These results highlight the potential applicability of the described framework for regions where measured data are scarce as well as where accurate and consistent soil moisture estimates do not currently exist. A follow-on study to be explored based on the results of the described experiments is the routing of streamflow using modeled runoff to analyze the effect of soil moisture

490 assimilation on runoff and river discharge. Antecedent soil moisture conditions affect the soil permeability and infiltration capacity. Therefore, it is expected that improvements in soil moisture estimation could translate into improved streamflow estimates.

Appendix A: Soil texture and landcover across study domain

Table A1 presents the predominant soil texture and landcover classes and their respective percentages across the study domain

495 shown in Fig. 1.

Table A1. List of soil texture and landcover classes (and their respective percentages) found within the study domain presented in Fig. 1.

Soil texture			Landcover		
Class	no. of grid cells	% of total grid cells	Class	no. of grid cells	% of total grid cells
Sand	12528	4.04	Forest	43669	14.1
Loamy Sand	322	0.10	Shrublands	62654	20.2
Sandy Loam	18753	6.05	Savannas	4244	1.4
Silt Loam	2098	0.68	Grasslands	41306	13.3
Loam	188716	60.91	Croplands	67366	21.7
Sandy Clay Loam	14132	4.56	Urban/ Built-up	1269	0.4
Clay Loam	28885	9.32	Snow/Ice	1027	0.3
Silty Clay	35	0.01	Barren/Sparsely vegetated	78338	25.3
Clay	23048	7.44	Ocean	9952	3.2
Water	10805	3.49			
Other (ice/lakes/water bodies)	10503	3.39			

Appendix B: Statistical metrics

The following formulas were used to calculate the relevant statistics described in Sect. 4:

$$\text{Bias} = \sum_{t=1}^{T}(y_s - y_m) \tag{B1}$$

500 $$\text{RMSE} = \sqrt{\frac{\sum_{t=1}^{T}(y_s - y_m)^2}{T}} \tag{B2}$$

$$\text{Unbiased RMSE} = \sqrt{\frac{\sum_{t=1}^{T}((y_s - \overline{(y_s - y_m)}) - y_m)^2}{T}} \tag{B3}$$

$$\text{Relative RMSE} = \frac{\text{RMSE}}{\sigma_{y_s}} \tag{B4}$$

505 $$\text{Confidence interval}_{95\%} \text{ limits} = \pm 1.96 * \frac{\sigma_X}{\sqrt{N}} \tag{B5}$$

where y_s equals the ensemble mean of the OL/DA-CDF/DA-NoCDF soil moisture estimate, y_m is the in situ soil moisture measurement, σ_{y_s} is the standard deviation of the ensemble mean soil moisture over time, T is the total number of data instances in time at a given location in space, X is the array containing bias/RMSE values computed for each comparative

510 grid cell, and N is the total number of (in situ measurements versus modeled estimates) comparative grid cells. The overbar represents temporally averaged values. The cross-correlation, R, between variables x and y is computed as:

$$\text{R} = \frac{\sum_{t=1}^{T}(x - \bar{x})(y - \bar{y})}{\sqrt{\sum_{t=1}^{T}(x - \bar{x})^2 \sum_{t=1}^{T}(y - \bar{y})^2}} \tag{B6}$$

The fractional normalized information content, NIC_{RMSE}, improved in terms of RMSE due to assimilation is computed as:

$$\text{NIC}_{RMSE} = \frac{\text{RMSE}_{OL} - \text{RMSE}_{DA}}{\text{RMSE}_{OL}} \tag{B7}$$

515 where RMSE_{OL} is the root mean squared error (RMSE) for the OL and RMSE_{DA} is the RMSE for the DA-CDF or DA-NoCDF experiment.

Acronyms and abbreviations

ALEXI	Atmosphere-Land Exchange Inverse
CDF	Cumulative distribution function
DA	Data assimilation
DA-CDF	Data assimilation with CDF matching
DA-NoCDF	Data assimilation without CDF matching
EnKF	Ensemble Kalman filter
ET	Evapotranspiration
GMIA	Global Map of Irrigation Areas

GOME-2	Global Ozone Monitoring Experiment 2
GPP	Gross primary production
IMERG	Integrated Multi-satellite Retrievals for Global Precipitation Measurement
L1	Layer 1 near-surface soil moisture
L2	Layer 2 root-zone soil moisture
LIS	Land Information System
MODIS	Moderate Resolution Imaging Spectroradiometer
MERRA2	Modern-Era Retrospective analysis for Research and Applications
NI	Normalized innovation
SIF	Solar-induced fluorescence
SM	Soil moisture
SMAP	Soil Moisture Active Passive
OL	Open loop
VOD	Vegetation optical depth

Code and data availability. The NASA Land Information System source code was downloaded from https://github.com/NASA-LIS/LISF. SMAP soil moisture retrievals were downloaded from https://nsidc.org/data/SPL3SMP/. Soil moisture measurements across the Tibetan

520 Plateau are available at https://ismn.earth/en/. FluxSAT Gross Primary Production is available at https://avdc.gsfc.nasa.gov/pub/tmp/FluxSat_GPP/. GOME-2 Fluorescence dataset can be downloaded from https://avdc.gsfc.nasa.gov/pub/data/satellite/MetOp/GOME_F/.

Author contributions. J.A.A. conducted the described experiments and compiled the manuscript; B.A.F. served as Co-Investigator to the project, contributed to the development of the study methodology, and helped edit the manuscript; S.V.K. served as the Principle Investigator to the project, developed the NASA Land Information Software platform used to run the assimilation experiments, and contributed to the

525 selection and acquiring of evaluation datasets.

Competing interests. The authors declare that there are no competing interests present

Acknowledgements. The authors would like to extend their gratitude to Dr. Yonghwan Kwon and Dr. David Mocko for providing guidance in setting up the NASA LIS assimilation framework. Additional thanks are extended to Dr. Christopher Hain and Dr. Martha Anderson for sharing the ALEXI dataset. Funding for this study was provided by the NASA Understanding Changes in High Mountain Asia contract

530 (80NSSC2OK1531), while the high-performance computing facility at the University of Maryland provided the super-computing platform to run the assimilation experiments.

References

Al-Kayssi, A., Al-Karaghouli, A., Hasson, A., and Beker, S.: Influence of soil moisture content on soil temperature and heat storage under greenhouse conditions, Journal of Agricultural Engineering Research, 45, 241–252, 1990.

535   Anderson, M. C., Norman, J. M., Mecikalski, J. R., Otkin, J. A., and Kustas, W. P.: A climatological study of evapotranspiration and moisture stress across the continental United States based on thermal remote sensing: 1. Model formulation, Journal of Geophysical Research: Atmospheres, 112, 2007.

Anderson, M. C., Kustas, W. P., Norman, J. M., Hain, C. R., Mecikalski, J. R., Schultz, L., González-Dugo, M., Cammalleri, C., d'Urso, G., Pimstein, A., et al.: Mapping daily evapotranspiration at field to continental scales using geostationary and polar orbiting satellite imagery,

540   Hydrology and Earth System Sciences, 15, 223–239, 2011.

Armstrong, R. L., Rittger, K., Brodzik, M. J., Racoviteanu, A., Barrett, A. P., Khalsa, S.-J. S., Raup, B., Hill, A. F., Khan, A. L., Wilson, A. M., et al.: Runoff from glacier ice and seasonal snow in High Asia: separating melt water sources in river flow, Regional Environmental Change, pp. 1–13, 2018.

Arsenault, K. R., Kumar, S. V., Geiger, J. V., Wang, S., Kemp, E., Mocko, D. M., Beaudoing, H. K., Getirana, A., Navari, M., Li, B., and

545   Jacob, J.: The Land surface Data Toolkit (LDT v7. 2)–a data fusion environment for land data assimilation systems, Geoscientific Model Development, 11, 3605–3621, 2018.

Asoka, A., Gleeson, T., Wada, Y., and Mishra, V.: Relative contribution of monsoon precipitation and pumping to changes in groundwater storage in India, Nature Geoscience, 10, 109–117, 2017.

Ball, J. T., Woodrow, I. E., and Berry, J. A.: A model predicting stomatal conductance and its contribution to the control of photosynthesis

550   under different environmental conditions, in: Progress in Photosynthesis Research, pp. 221–224, Springer, 1987.

Biemans, H., Siderius, C., Mishra, A., and Ahmad, B.: Crop-specific seasonal estimates of irrigation-water demand in South Asia, Hydrology and Earth System Sciences, 20, 1971–1982, 2016.

Brodzik, M. J., Billingsley, B., Haran, T., Raup, B., and Savoie, M. H.: EASE-Grid 2.0: Incremental but significant improvements for Earth-gridded data sets, ISPRS International Journal of Geo-Information, 1, 32–45, 2012.

555   Brutsaert, W.: Evaporation into the atmosphere: theory, history and applications, vol. 1, Springer Science & Business Media, 2013.

Buehner, M.: Error statistics in data assimilation: estimation and modelling, in: Data Assimilation, pp. 93–112, Springer, 2010.

Chambers, R.: Managing canal irrigation: practical analysis from South Asia, Cambridge University Press, 1988.

Daly, E. and Porporato, A.: A review of soil moisture dynamics: from rainfall infiltration to ecosystem response, Environmental Engineering Science, 22, 9–24, 2005.

560   Dhar, O. and Nandargi, S.: Hydrometeorological aspects of floods in India, Natural Hazards, 28, 1–33, 2003.

Douville, H., Chauvin, F., and Broqua, H.: Influence of soil moisture on the Asian and African monsoons. Part I: Mean monsoon and daily precipitation, Journal of Climate, 14, 2381–2403, 2001.

Dukes, M. and Scholberg, J.: Soil moisture controlled subsurface drip irrigation on sandy soils, Applied Engineering in Agriculture, 21, 89–101, 2005.

565   Ek, M., Mitchell, K., Lin, Y., Rogers, E., Grunmann, P., Koren, V., Gayno, G., and Tarpley, J.: Implementation of Noah land surface model advances in the National Centers for Environmental Prediction operational mesoscale ETA model, Journal of Geophysical Research: Atmospheres, 108, 2003.

Entekhabi, D., Njoku, E. G., O'Neill, P. E., Kellogg, K. H., Crow, W. T., Edelstein, W. N., Entin, J. K., Goodman, S. D., Jackson, T. J., Johnson, J., et al.: The soil moisture active passive (SMAP) mission, Proceedings of the IEEE, 98, 704–716, 2010.

570 Farr, T. G., Rosen, P. A., Caro, E., Crippen, R., Duren, R., Hensley, S., Kobrick, M., Paller, M., Rodriguez, E., Roth, L., and Seal, D.: The shuttle radar topography mission, Reviews of Geophysics, 45, 2007.

Friedl, M. A., McIver, D. K., Hodges, J. C., Zhang, X. Y., Muchoney, D., Strahler, A. H., Woodcock, C. E., Gopal, S., Schneider, A., Cooper, A., and Baccini, A.: Global land cover mapping from MODIS: algorithms and early results, Remote Sensing of Environment, 83, 287–302, 2002.

575 Gelaro, R., McCarty, W., Suárez, M. J., Todling, R., Molod, A., Takacs, L., Randles, C. A., Darmenov, A., Bosilovich, M. G., Reichle, R., and Wargan, K.: The modern-era retrospective analysis for research and applications, version 2 (MERRA-2), Journal of Climate, 30, 5419–5454, 2017.

Girotto, M., De Lannoy, G. J., Reichle, R. H., Rodell, M., Draper, C., Bhanja, S. N., and Mukherjee, A.: Benefits and pitfalls of GRACE data assimilation: A case study of terrestrial water storage depletion in India, Geophysical Research Letters, 44, 4107–4115, 2017.

580 Gough, C.: Terrestrial Primary Production: Fuel for, Nature Education Knowledge, 3(10):28, 2011.

Green, J. K., Seneviratne, S. I., Berg, A. M., Findell, K. L., Hagemann, S., Lawrence, D. M., and Gentine, P.: Large influence of soil moisture on long-term terrestrial carbon uptake, Nature, 565, 476–479, 2019.

Gutman, G. and Ignatov, A.: The derivation of the green vegetation fraction from NOAA/AVHRR data for use in numerical weather prediction models, International Journal of Remote Sensing, 19, 1533–1543, 1998.

585 Hauser, M., Orth, R., and Seneviratne, S. I.: Investigating soil moisture–climate interactions with prescribed soil moisture experiments: an assessment with the Community Earth System Model (version 1.2), Geoscientific Model Development, 10, 1665–1677, 2017.

Huang, C., Li, X., Lu, L., and Gu, J.: Experiments of one-dimensional soil moisture assimilation system based on ensemble Kalman filter, Remote Sensing of Environment, 112, 888–900, 2008.

Huffman, G. J., Bolvin, D. T., Braithwaite, D., Hsu, K., Joyce, R., Xie, P., and Yoo, S.-H.: NASA global precipitation measurement (GPM)

590 integrated multi-satellite retrievals for GPM (IMERG), Algorithm Theoretical Basis Document (ATBD) Version, 4, 26, 2015.

Jalilvand, E., Tajrishy, M., Hashemi, S. A. G. Z., and Brocca, L.: Quantification of irrigation water using remote sensing of soil moisture in a semi-arid region, Remote Sensing of Environment, 231, 111 226, 2019.

Joiner, J. and Yoshida, Y.: Satellite-based reflectances capture large fraction of variability in global gross primary production (GPP) at weekly time scales, Agricultural and Forest Meteorology, 291, 108 092, 2020.

595 Joiner, J., Guanter, L., Lindstrot, R., Voigt, M., Vasilkov, A., Middleton, E., Huemmrich, K., Yoshida, Y., and Frankenberg, C.: Global monitoring of terrestrial chlorophyll fluorescence from moderate-spectral-resolution near-infrared satellite measurements: methodology, simulations, and application to GOME-2, Atmospheric Measurement Techniques, 6, 2803–2823, 2013.

Joiner, J., Yoshida, Y., Vasilkov, A., Schaefer, K., Jung, M., Guanter, L., Zhang, Y., Garrity, S., Middleton, E., Huemmrich, K., and Gu, L.: The seasonal cycle of satellite chlorophyll fluorescence observations and its relationship to vegetation phenology and ecosystem atmosphere

600 carbon exchange, Remote Sensing of Environment, 152, 375–391, 2014.

Jordan, R.: A one-dimensional temperature model for a snow cover: Technical documentation for SNTHERM. 89., Tech. rep., Cold Regions Research and Engineering Lab, Hanover NH, 1991.

Kalman, R. E.: A new approach to linear filtering and prediction problems, Journal of Basic Engineering, 82, 35–45, https://doi.org/10.1115/1.3662552, 1960.

605 Knipper, K. R., Kustas, W. P., Anderson, M. C., Alfieri, J. G., Prueger, J. H., Hain, C. R., Gao, F., Yang, Y., McKee, L. G., Nieto, H., et al.: Evapotranspiration estimates derived using thermal-based satellite remote sensing and data fusion for irrigation management in California vineyards, Irrigation Science, 37, 431–449, 2019.

Kumar, S., Peters-Lidard, C., Santanello, J., Reichle, R., Draper, C., Koster, R., Nearing, G., and Jasinski, M.: Evaluating the utility of satellite soil moisture retrievals over irrigated areas and the ability of land data assimilation methods to correct for unmodeled processes,
610 Hydrology and Earth System Sciences, 19, 4463–4478, 2015.

Kumar, S. V., Peters-Lidard, C. D., Tian, Y., Houser, P. R., Geiger, J., Olden, S., Lighty, L., Eastman, J. L., Doty, B., Dirmeyer, P., and Adams, J.: Land information system: an interoperable framework for high resolution land surface modeling, Environmental Modelling & Software, 21, 1402–1415, 2006.

Kumar, S. V., Holmes, T. R., Bindlish, R., Jeu, R. d., and Peters-Lidard, C.: Assimilation of vegetation optical depth retrievals from passive
615 microwave radiometry, Hydrology and Earth System Sciences, 24, 3431–3450, 2020.

Kwon, Y., Forman, B. A., Ahmad, J. A., Kumar, S. V., and Yoon, Y.: Exploring the Utility of Machine Learning-Based Passive Microwave Brightness Temperature Data Assimilation over Terrestrial Snow in High Mountain Asia, Remote Sensing, 11, 2265, 2019.

Lievens, H., Tomer, S. K., Al Bitar, A., De Lannoy, G. J., Drusch, M., Dumedah, G., Franssen, H.-J. H., Kerr, Y. H., Martens, B., Pan, M., and Roundy, J.: SMOS soil moisture assimilation for improved hydrologic simulation in the Murray Darling Basin, Australia, Remote
620 Sensing of Environment, 168, 146–162, 2015.

Loomis, B. D., Richey, A. S., Arendt, A. A., Appana, R., Deweese, Y.-J., Forman, B. A., Kumar, S. V., Sabaka, T. J., and Shean, D. E.: Water storage trends in high mountain Asia, Frontiers in Earth Science, 7, 235, 2019.

McCuen, R. H.: Modeling hydrologic change: statistical methods, CRC press, 2016.

McLaughlin, D.: An integrated approach to hydrologic data assimilation: interpolation, smoothing, and filtering, Advances in Water Re-
625 sources, 25, 1275–1286, 2002.

Morin, J. and Benyamini, Y.: Rainfall infiltration into bare soils, Water Resources Research, 13, 813–817, 1977.

Natural Resources Conservation Service: United States Department of Agriculture. Web Soil Survey, http://websoilsurvey.nrcs.usda.gov/.

Nearing, G., Yatheendradas, S., Crow, W., Zhan, X., Liu, J., and Chen, F.: The efficiency of data assimilation, Water resources research, 54, 6374–6392, 2018.

630 Niu, G.-Y. and Yang, Z.-L.: Effects of frozen soil on snowmelt runoff and soil water storage at a continental scale, Journal of Hydrometeo-rology, 7, 937–952, 2006.

Niu, G.-Y., Yang, Z.-L., Dickinson, R. E., Gulden, L. E., and Su, H.: Development of a simple groundwater model for use in climate models and evaluation with Gravity Recovery and Climate Experiment data, Journal of Geophysical Research: Atmospheres, 112, 2007.

Niu, G.-Y., Yang, Z.-L., Mitchell, K. E., Chen, F., Ek, M. B., Barlage, M., Kumar, A., Manning, K., Niyogi, D., Rosero, E., and Tewari,
635 M.: The community Noah land surface model with multiparameterization options (Noah-MP): 1. Model description and evaluation with local-scale measurements, Journal of Geophysical Research: Atmospheres, 116, 2011.

O'Neill, P., Chan, S., Njoku, E., Jackson, T., and Bindlish, R.: Soil moisture active passive (SMAP) algorithm theoretical basis document: level 2 & 3 soil moisture (passive) data products, Tech. rep., Jet Propulsion Laboratory. California Institute of Technology, 2014.

O'Neill, P., Chan, S., Njoku, E., Jackson, T., and Bindlish, R.: SMAP L3 Radiometer Global Daily 36 km EASE-Grid Soil Moisture, Version
640 6, https://doi.org/10.5067/EVYDQ32FNWTH, 2019.

Panciera, R., Walker, J. P., Jackson, T. J., Gray, D. A., Tanase, M. A., Ryu, D., Monerris, A., Yardley, H., Rüdiger, C., Wu, X., et al.: The soil moisture active passive experiments (SMAPEx): toward soil moisture retrieval from the SMAP mission, IEEE Transactions on Geoscience and Remote Sensing, 52, 490–507, 2013.

Penna, D., Tromp-van Meerveld, H., Gobbi, A., Borga, M., and Dalla Fontana, G.: The influence of soil moisture on threshold runoff generation processes in an alpine headwater catchment, Hydrology and Earth System Sciences, 15, 689–702, 2011.

Peters-Lidard, C. D., Houser, P. R., Tian, Y., Kumar, S. V., Geiger, J., Olden, S., Lighty, L., Doty, B., Dirmeyer, P., Adams, J., and Mitchell, K.: High-performance Earth system modeling with NASA/GSFC's Land Information System, Innovations in Systems and Software Engineering, 3, 157–165, 2007.

Philander, S. G.: Encyclopedia of global warming and climate change: AE, vol. 1, Sage, 2008.

Piles, M., Camps, A., Vall-Llossera, M., Corbella, I., Panciera, R., Rudiger, C., Kerr, Y. H., and Walker, J.: Downscaling SMOS-derived soil moisture using MODIS visible/infrared data, IEEE Transactions on Geoscience and Remote Sensing, 49, 3156–3166, 2011.

Reichle, R. H. and Koster, R. D.: Bias reduction in short records of satellite soil moisture, Geophysical Research Letters, 31, 2004.

Reichle, R. H., Koster, R. D., Dong, J., and Berg, A. A.: Global soil moisture from satellite observations, land surface models, and ground data: Implications for data assimilation, Journal of Hydrometeorology, 5, 430–442, 2004.

Reichle, R. H., Liu, Q., Ardizzone, J. V., Crow, W. T., De Lannoy, G. J., Dong, J., Kimball, J. S., and Koster, R. D.: The contributions of gauge-based precipitation and SMAP brightness temperature observations to the skill of the SMAP Level-4 soil moisture product, Journal of Hydrometeorology, 22, 405–424, 2021.

Robinson, D. A. and Kukla, G.: Maximum surface albedo of seasonally snow-covered lands in the Northern Hemisphere, Journal of Climate and Applied Meteorology, 24, 402–411, 1985.

Rodell, M., Velicogna, I., and Famiglietti, J. S.: Satellite-based estimates of groundwater depletion in India, Nature, 460, 999–1002, 2009.

Schneider, S. H.: The greenhouse effect: science and policy, Science, 243, 771–781, 1989.

Seneviratne, S. I., Corti, T., Davin, E. L., Hirschi, M., Jaeger, E. B., Lehner, I., Orlowsky, B., and Teuling, A. J.: Investigating soil moisture–climate interactions in a changing climate: A review, Earth-Science Reviews, 99, 125–161, 2010.

Shani, U., Tsur, Y., and Zemel, A.: Optimal dynamic irrigation schemes, Optimal Control Applications and Methods, 25, 91–106, 2004.

Siebert, S., Döll, P., Hoogeveen, J., Faures, J.-M., Frenken, K., and Feick, S.: Development and validation of the global map of irrigation areas, Hydrology and Earth System Sciences, 9, 535–547, 2005.

Sivakumar, M. V. and Stefanski, R.: Climate change in *S*outh *A*sia, in: Climate change and food security in South Asia, pp. 13–30, Springer, 2010.

Soulis, K. X., Elmaloglou, S., and Dercas, N.: Investigating the effects of soil moisture sensors positioning and accuracy on soil moisture based drip irrigation scheduling systems, Agricultural Water Management, 148, 258–268, 2015.

Su, Z., Wen, J., Dente, L., Velde, R., Wang, L., Ma, Y., Yang, K., and Hu, Z.: The Tibetan Plateau observatory of plateau scale soil moisture and soil temperature (Tibet-Obs) for quantifying uncertainties in coarse resolution satellite and model products, Hydrology and Earth System Sciences, 15, 2303–2316, 2011.

Van der Tol, C., Berry, J., Campbell, P., and Rascher, U.: Models of fluorescence and photosynthesis for interpreting measurements of solar-induced chlorophyll fluorescence, Journal of Geophysical Research: Biogeosciences, 119, 2312–2327, 2014.

Wei, J. and Dirmeyer, P. A.: Dissecting soil moisture-precipitation coupling, Geophysical Research Letters, 39, 2012.

Wester, P., Mishra, A., Mukherji, A., and Shrestha, A. B.: The Hindu Kush Himalaya Assessment- Mountains, Climate Change, Sustainability and People, Springer Nature Switzerland, 2018.

Yang, K., Qin, J., Zhao, L., Chen, Y., Tang, W., Han, M., Chen, Z., Lv, N., Ding, B., Wu, H., and Lin, C.: A multiscale soil moisture and
680   freeze–thaw monitoring network on the third pole, Bulletin of the American Meteorological Society, 94, 1907–1916, 2013.

Yang, Z.-L. and Dickinson, R. E.: Description of the Biosphere-Atmosphere Transfer Scheme (BATS) for the soil moisture workshop and
       evaluation of its performance, Global and Planetary Change, 13, 117–134, 1996.

Yang, Z.-L., Niu, G.-Y., Mitchell, K. E., Chen, F., Ek, M. B., Barlage, M., Longuevergne, L., Manning, K., Niyogi, D., Tewari, M., and
       Xia, Y.: The community Noah land surface model with multiparameterization options (Noah-MP): 2. Evaluation over global river basins,
685   Journal of Geophysical Research: Atmospheres, 116, 2011.

Zeng, Y., Su, Z., Van der Velde, R., Wang, L., Xu, K., Wang, X., and Wen, J.: Blending satellite observed, model simulated, and in situ
       measured soil moisture over Tibetan Plateau, Remote Sensing, 8, 268, 2016.

Zhang, D., Tang, R., Zhao, W., Tang, B., Wu, H., Shao, K., and Li, Z.-L.: Surface soil water content estimation from thermal remote sensing
       based on the temporal variation of land surface temperature, Remote Sensing, 6, 3170–3187, 2014.

690   Zhang, Z. and Moore, J. C.: Mathematical and Physical Fundamentals of Climate Change, Elsevier, 2015.